



CIVIL ENGINEERING STUDIES
Illinois Center for Transportation Series No. ICT-17-004
UILU-ENG- UILU-ENG-2017-2004
ISSN: 0197-9191

NUMERICAL PREDICTION OF THREE-DIMENSIONAL TIRE- PAVEMENT CONTACT STRESSES

Prepared By
Jaime A. Hernandez
Angeli Gamez
Maryam Shakiba
Imad L. Al-Qadi
University of Illinois at Urbana-Champaign

Research Report No. ICT-17-004

A report of the findings of
ICT PROJECT ICT-17-004

**NUMERICAL PREDICTION OF THREE-DIMENSIONAL
TIRE-PAVEMENT CONTACT STRESSES**

Illinois Center for Transportation
April 2015

ACKNOWLEDGMENT AND DISCLAIMER

The project that is the subject of this report was done under contract for Texas A&M University. The contents of this report reflect the view of the authors, who are responsible for the facts and the accuracy of the data presented herein. The contents do not necessarily reflect the official views or policies of the Illinois Center for Transportation, the Illinois Department of Transportation, or the Federal Highway Administration. This report does not constitute a standard, specification, or regulation. Any inclusion of manufacturer names, trade names, or trademarks is for identification purposes only and is not to be considered an endorsement. Each contract report is peer reviewed and accepted for publication by Research Council staff with expertise in related technical areas. Final editing and proofreading of the report are performed by the contractor.

EXECUTIVE SUMMARY

Several research and studies confirmed that tires with the same vehicle loading but different conditions and configurations induce different stresses on pavement surfaces. The produced complex contact stresses have significant effects on the pavement response and performance. However, the lack of scientific quantification of the generated interactions between tires and pavements caused misrepresentation of pavement response in simulations and studies. Therefore, it is necessary to develop new approach and models to accurately predict the contact stresses induced by the tire on the pavement under different conditions. The results obtained from tire modeling should be used as realistic boundary conditions to simulate and predict pavement response.

The objective of this study is to develop a numerical modeling to simulate tires and investigate the effects of different tire and vehicle conditions on tire-pavement interactions. A three-dimensional (3-D) finite element (FE) representation of a dual-tire assembly is constructed to predict tire-pavement contact stress distributions. The tire is considered as a composite structure, including rubber and reinforcements. The tire material properties are calibrated based on the experimental measurement and data provided by tire manufacturer. The tire rolling process at different states is simulated using the arbitrary Lagrangian-Eulerian (ALE) formulation. Slide-velocity-dependent friction coefficient is used in the modeling. The constructed tire FE representation is calibrated and validated with experimental measurements of contact area, deflection, and maximum vertical contact stress. The developed FE tire-pavement interaction model is used to evaluate the contact area and mechanism of contact stress distributions at the tire-pavement interface under various tire and vehicle conditions.

The distribution of contact stresses at the tire-pavement interface under different vehicle loading and speed, tire inflation pressure, vehicle maneuvering (braking, acceleration, and steady state), and rolling conditions are studied. The results clearly demonstrate the existence of non-uniform vertical contact stresses and localized tangential contact stresses at the tire-pavement interface. Investigations of the effects of applied load and tire inflation pressure show that the non-uniformity of vertical contact stresses decreases as the load increases, but increases as the inflation pressure increases. Vehicle speed does not significantly affect the vertical contact stresses. However, vehicle-maneuvering behavior significantly affects tire-pavement contact stress distributions. Tire braking/acceleration induces significant longitudinal contact stresses, while tire cornering causes the peak contact stresses to shift towards one side of the contact patch.

The numerical results observed provide valuable insights into understanding realistic tire-pavement interactions. These complex responses indicate the importance of applying a realistic distribution of contact stresses on pavements to accurately predict pavement responses. The numerical results in this work provide the mechanistic analysis of pavement responses, such as PANDA, with realistic loading boundary conditions. The obtained 3-D contact stresses under various conditions in this study are incorporated into PANDA User Interface (PUI) to automatically generate pavement FE input file with realistic loading boundary conditions.

TABLE OF CONTENTS

	Page
Acknowledgement and Disclaimer	i
Executive Summary	ii
Table of Contents	iii
List of Tables	iv
List of Figures	v
1 Introduction	7
1.1 Problem Statement	7
1.2 Background	8
1.3 Objectives	10
1.4 Research Approach and Scope	10
2 Contact stress measurements	13
2.1 Measuring Equipment and Experimental Program	13
2.2 Three-Dimensional Contact Stresses	14
2.3 Contact Area and Load-Deflection Curves	17
3 Numerical modeling	18
3.1 Modeling Approach	18
3.2 Geometry of the Finite Element Model	19
3.3 Characterization of Tire Materials	21
3.4 Optimized Mesh for the Finite Element Model	23
3.5 Calibration and Validation of Numerical Model	25
4 Analysis of contact stresses	27
4.1 Accelerating Scenario	30
4.2 Braking Scenario	32
4.3 Cornering Scenario	33
5 Implementation of contact stresses into PANDA	36
5.1 Revised Features	36
5.2 Algorithm and Approach	39
5.3 Implementation	43
6 Findings and Conclusions	45
7 References	47

LIST OF TABLES

	Page
Table 3-1. Reinforcement details	20
Table 3-2. Mooney-Rivlin constants for rubber components	22

LIST OF FIGURES

	Page
Figure 1-1. Schematic representation of tire basics (from Michelin website on November 6 th 2014).	9
Figure 1-2. The matrix of conducted FE simulations to produce tire-induced contact stresses on the pavement under various conditions.	11
Figure 1-3. A sample representation of (a) revised PUI and (b) a generated FE input file with modified elements width and applied non-uniform 3-D contact stresses.....	12
Figure 2-1. Measuring system and tested tire.	13
Figure 2-2. Three best replicates and detail of filter process outcome.	14
Figure 2-3. Typical variation of 3-D contact stresses along the contact length (σ_x represents longitudinal, σ_y transverse, and σ_z vertical contact stresses).	14
Figure 2-4. Variation of maximum vertical contact stresses, σ_z, max , across tire under different applied load, P	15
Figure 2-5. Magnitude of normalized maximum transverse contact stress, σ_y, max , with respect to maximum normalized vertical contact stress, σ_z, max	16
Figure 2-6. Magnitude of normalized maximum longitudinal contact stress, σ_x, max , with respect to maximum normalized vertical contact stress, σ_z, max	16
Figure 2-7. Contact area and load-deflection curves.	17
Figure 3-1. Analysis stages.	18
Figure 3-2. Friction coefficient vs. vehicle velocity based on Wang (2013) friction model.....	19
Figure 3-3. Tire's (DTA 275/80R22.5) dimension in the cross section.	21
Figure 3-4. Stress-strain curve for Belt 1.....	22
Figure 3-5. Mesh configuration considered in the half-axisymmetric model.....	23
Figure 3-6. Variation of normalized total strain energy, E , with number of elements, N	24
Figure 3-7. Variation of normalized total strain energy with number of elements along the (a) foot and (b) region with cylindrical elements.....	24
Figure 3-8. Measured vs. calculated (a) contact area, (b) deflection, and (c) maximum contact stresses.....	26
Figure 4-1. Analysis matrix of the DTA simulations on a rigid surface.....	27
Figure 4-2. Contact stress variation along the contact length of a free-rolling tire varying velocities ($V1 = 8, V2 = 65, V3 = 115 \text{ km/h}$) in the (a) vertical, (b) longitudinal, (c) transverse directions.	29
Figure 4-3. Typical contact stress variation of an accelerating tire with $V = 8 \text{ km/h}$, $P = 44.4 \text{ kN}$, and $\sigma_0 = 690 \text{ kPa}$ in the (a) vertical, (b) longitudinal, and (c) transverse directions.....	31
Figure 4-4. Typical contact stress variation of a braking tire with $V = 8 \text{ km/h}$, $P = 44.4 \text{ kN}$, and $\sigma_0 = 690 \text{ kPa}$ in the (a) vertical, (b) longitudinal, and (c) transverse directions.....	32

Figure 4-5. Typical contact stress variation of a cornering tire with $V = 8 \text{ km/h}$, $P = 44.4 \text{ kN}$, and $\sigma_0 = 690 \text{ kPa}$ in the (a) vertical, (b) longitudinal, and (c) transverse directions.....	34
Figure 4-6. Vertical force distribution carried by each meridian for a cornering tire with $\sigma_0 = 552 \text{ kPa}$ and $V = 8 \text{ km/h}$ with varying applied loads.	34
Figure 5-1. The main window of PUI in the (a) previous version and (b) new version to select analysis and loading types.	37
Figure 5-2. The load tab of PUI in the (a) previous version and (b) new version to select load and contact area.....	38
Figure 5-3. Available options of PUI to choose (a) tire load, (b) tire pressure, (c) vehicle speed, (d) rolling conditions, and (e) slip ratio.....	39
Figure 5-4. Longitudinal dimensions of the finite element model.....	40
Figure 5-5. Characteristics of FE model for uniform moving load, (a) four-layer pavement FE model, (b) uniform meshing under the wheel path, (c) uniform vertical pressure on the surface, and (d) 13 different defined sets for applied load.	41
Figure 5-6. Characteristics of the FE model for 3-D non-uniform moving load, (a) four-layer pavement FE model, (b) non-uniform meshing under the wheel path, (c) 3-D non-uniform contact stresses on the surface, and (d) +1000 defined sets for non-uniform contact stresses to be applied on.	42
Figure 5-7. Part of the modified visual studio code demonstrating an explanation comment and an if-clause modifying elements width value.....	43
Figure 5-8. A Visual Studio code defining new sets to applied non-uniform load.	43
Figure 5-9. A Visual Studio code defining (a) vertical non-uniform pressure on defined sets, (b) non-uniform longitudinal traction on defined sets, and (c) concatenating the produced lines in (a) and (b) to be written in FE input file.	44

1 INTRODUCTION

1.1 PROBLEM STATEMENT

To accurately predict pavement response and performance, the realistic loading boundary conditions need to be applied on pavements. Tire induces contact stresses on pavement because of moving vehicle load, which depends on tire geometry and loading conditions. Experimental studies measurement demonstrated that the tire contact stresses are three-dimensional (3-D) and highly non-uniform. The bending stiffness within the tire structure produces non-uniform vertical contact stresses. The transverse contact stresses develop as a result of restricted inward movement of the tire ribs, and the friction between tire and pavement mainly causes the longitudinal tire contact stresses (Tielking and Roberts, 1987). These tire-pavement contact stresses change with different applied load, inflation pressure, vehicle speed, and mode (Yap, 1988).

The 3-D non-uniform contact stresses on pavement surfaces increase pavement damage, which includes top-down cracking, near-surface cracking, and hot-mix asphalt (HMA) rutting. Many researchers analyzed the effect of the 3-D non-uniform stresses on flexible pavement response and emphasized their importance. Siddharthan et al. (2002) compared the response of pavement under uniform and non-uniform tire contact stress distributions. They concluded that the use of conventional uniform load distribution estimates inaccurate response of pavement rutting. De Beer et al. (2002) found that pavement responses of thin HMA pavements are sensitive to vertical load shape and distribution. Drakos et al. (2001) concluded that the 3-D tire contact stresses increase HMA rutting potential. Romanoschi and Metcalf (2001), Al-Qadi and Yoo (2007), Wang and Al-Qadi (2009), and Wang and Al-Qadi (2010) reported that the effect of surface tangential stresses on pavement response is significant. They concluded that when horizontal, surface tangential stresses are incorporated, the potential of surface-initiated top-down cracking increases in the pavement surface near the edge of the tire. They also observed that the horizontal tangential stress, which can be as high as half of the vertical compressive stress, affects pavement response and should be considered in pavement analysis.

Over the past few years, researchers at Texas A&M University developed the Pavement Analysis using Nonlinear Damage Approach (PANDA) (Masad et al., 2012). PANDA includes significant improvements regarding the use of material characteristics and nonlinear finite element method to analyze and design pavement structures. Nonlinear coupled thermo- viscoelastic, viscoplastic, viscodamage, and healing response of asphalt concrete are considered in PANDA (Darabi et al., 2011). PANDA User Interface (PUI) is also developed to provide a friendly interface for a user to construct the FE input file. However, PUI receives the contact area and applied load from the user and applies a uniform vertical pressure on pavements. In order to obtain a more accurate response of asphalt pavement using PANDA, it is imperative that PUI applies a realistic distribution of 3-D tire contact stresses on pavements.

Two approaches can be used to measure tire-pavement contact stresses: experimental measurements and tire simulations. The Council for Scientific and Industrial Research (CSIR) in South Africa (Bonse and Kuhn, 1959) developed a device, which measured forces in the three principal directions. The measurements demonstrated that vertical stresses are primarily affected by tire inflation pressure and longitudinal stresses by tire torque. Different apparatus were

constructed since then to measure tire contact stresses (Seitz and Hussmann, 1971; Lippmann and Oblizajek, 1974; Howell et al., 1986; Tielking and Abraham, 1994; Himeno et al., 1997; Anghelache et al., 2003). Recently, Anghelache et al. (2011) constructed a measuring device composed of steel-sensing elements with resistive strain gauges (10×10 mm square contact area). This device measures contact stresses under different rolling conditions. Despite the improvements in measuring devices, experimental measurements can provide the contact area and applied stresses resulting from a slow moving tire on rigid sensors and are time consuming and expensive. Extending these measurements to other tire types and moving conditions (varying speed, braking, and acceleration) is difficult. Therefore, air-inflated tire models using FE simulations should be used as an alternative approach. Such tire FE models should consider all features of tire geometry (tread width, contact area, curvatures, etc.) and predict 3-D contact stresses as a result of steady-state moving, accelerating, and braking conditions. The tire models can be validated using experimental measurements, including contact area and contact stress of a slow moving truck tire.

This work presents a numerical approach to simulate a realistic FE representation of tire and provide the comparative stress distributions under various tire loading and rolling conditions. The results provide a comprehensive insight into stress distributions at the tire-pavement interface. The contact stresses obtained are then implemented in PUI to grant the user the option of choosing realistic tire loading on pavements. In the following, a comprehensive literature review is presented on tire-pavement interactions FE modeling. Then, the objective and approach of this study are described.

1.2 BACKGROUND

FE commercial software, such as ABAQUS, ANSYS, and ADINA, has become popular in the tire and pavement industries in recent decades for simulating tire responses. The FE approach is a preferable method compared with simplified tire models because it considers the complex tire structure, material properties, and rolling conditions. Figure 1-1 schematically illustrates the basics of a tire structure. The outer structure is usually considered as rubber and the bead, crown ply, and carcass ply are considered as reinforcement in the FE representation of tires. The complexity of the available FE representations of tires varies depending on the characteristics of the developed model, including FE formulation (Lagrangian, Eulerian or the arbitrary Lagrangian- Eulerian, ALE), material models (linear elastic, hyperelastic or viscoelastic), type of time domain (transient or steady state) and type of analysis (isothermal, non-isothermal or thermo-mechanical). Depending on the purpose of the study analyzing tire-pavement interaction, steady-state or transient response, vibration and noise, tire failure, and rolling resistance, different combinations of FE features can be chosen.



Figure 1-1. Schematic representation of tire basics (from Michelin website on November 6th 2014).

Several researchers used the FE approach to study the effect of tire characteristics and conditions on the resultant tire contact area and stresses. To investigate the effect of inflation pressure and load on the resultant tire-induced contact stresses, Tielking and Roberts (1987) built an FE representation of a tire constructed using axisymmetric shell elements positioned along the carcass mid-ply surface; the pavement was considered a rigid flat surface. By simulating a simple strip model as a cross section of a tire, Roque et al. (2000) concluded that both vertical and lateral tire contact stresses measured on rigid foundations accurately represent the contact stresses for the same tire on typical asphalt pavement structures. Therefore, the contact stresses measured by devices with rigid foundations are suitable for predicting response and performance of highway pavements. Zhang et al. (2001) constructed a truck tire FE representation using ANSYS and analyzed the internal shear stresses between the belt and carcass layers as a function of applied loads and inflation pressures. Shoop (2001) developed a full 3-D representation of tire rolling over a deformable terrain. Fresh snow and compacted sand surfaces were modeled using critical-state plasticity models. He suggested that the assumption of a rigid tire might be a good approximation for soft terrain analysis. Meng (2002) used ABAQUS to simulate a tire on rigid pavement surface and analyzed the vertical contact stress distributions under various tire loading conditions. Ghoreishy et al. (2007) constructed a 3-D FE representation of a 155/65R13 steel-belted tire in ABAQUS. They examined the effect of some structural and operational parameters on the mechanical behavior of the tire under different inflation pressure, static load, and steady-state rolling conditions. The results demonstrated that the belt angle was the most important constructional variable for tire behavior, and the change of friction coefficient had great influence on the pressure field and relative shear between tire treads and road.

Wang and Roque (2010) constructed a 3-D tire-pavement interaction FE model using ADINA. All tire components were modeled as linear elastic materials (rubber and steel). The pavement was modeled as a relatively stiff single layer support. Material properties of the tire were back calculated to achieve good agreement between predicted and measured load-deflection curves. The load was assumed to be monotonically applied. The measured contact stresses and load-deflection curves from one radial truck tire were used to calibrate and validate the developed model. Gruber and his co-workers (Gruber et al., 2011a, b; Gruber and Sharp, 2012) first developed an FE model for a racing car tire. Then, they extended the model to study the carcass deflections, contact pressure, and shear stress distributions for a steady rolling, slipping, and cambered tire with special attention to heavy braking. They provided considerable insight into how the tire deforms and how the contact stresses are distributed as functions of the running conditions.

Wang et al.(2011) developed a 3-D FE model of an air-inflated ribbed tire, and the interaction between the tire and a non-deformable pavement surface was considered. All material properties in the model (tire and pavement) were assumed linear elastic and the load was statically applied. The model was calibrated with load-deflection curves. Various rolling conditions were analyzed and it was observed that the longitudinal contact stresses increase during braking. Wang et al. (2014) improved their previous work by including the velocity-dependent friction. They observed that longitudinal contact stresses were higher in braking and traction compared with free-rolling conditions, while the transverse contact stresses were smaller. Moreover, the in-plane contact stresses were greater during cornering compared with the contact stresses in free-rolling conditions. The results showed that the constant friction coefficient assumption is acceptable for free rolling but not for braking and traction.

However, the FE tire models available in the literature have not been thoroughly validated against experimental data. Therefore, in this study an FE representation of tire considering full geometry features with improved mesh was first constructed. In addition, the friction coefficient was considered a function of vehicle speed. The tire model was then calibrated and validated against experimental measurement by the Stress-In-Motion (SIM) devices obtained by CSIR in South Africa. Then, a comprehensive set of simulations, dictated by pavement design community needs and demands, were conducted to produce a database of tire contact stresses for application on pavements. The database includes contact stresses at various applied load, tire inflation pressure, vehicle speed, and rolling condition (accelerating, braking, and steady-state).

1.3 OBJECTIVES

PANDA, an FE code that uses state-of-the-art techniques for modeling nonlinear and damage behavior of asphalt concrete, requires realistic and accurate loading boundary conditions to predict accurate asphalt pavement response. The objective of this study is to provide realistic input of tire-pavement contact stresses under different tire and vehicle conditions for PANDA simulations.

For this purpose, a numerical approach was developed to simulate an FE representation of tire considering full tire geometry. The constructed model was calibrated and validated against experimental measurements. The finalized FE model was used to study the tire-induced contact stresses at braking, free rolling, and acceleration under different conditions of applied load, tire inflation pressure, and vehicle speed.

The contact stresses obtained are tabulated in such a way that can be used as load boundary conditions for any FE pavement model. The tabulated 3-D non-uniform contact stresses were implemented into PUI to be automatically incorporated into FE input file for PANDA.

1.4 RESEARCH APPROACH AND SCOPE

The main objective of this research is to investigate the contact stress distribution at the tire-pavement interface and incorporate it into PUI. To achieve this objective, the following research tasks were conducted:

- A 3-D FE model was developed for a Dual-Tire Assembly (DTA) to generate 3D non-uniform contact stresses. The FE representation of the DTA 275/80R22.5, considering full geometry features with optimized mesh, compared with the previous studies, was constructed. The tire was modeled as a composite structure, including rubber and reinforcement. The effect of pavement friction coefficient as a function of vehicle speed was also considered.
- Tire material properties were obtained based on laboratory testing and information from tire manufacturer. The FE model was then calibrated by the experimentally measured load-deflection curves and validated per the contact area, deflection, and maximum contact stresses, obtained from experimental measurements.
- Using the numerical model, a database of predicted contact stresses was produced. The database includes the distribution of non-uniform 3-D contact stresses under different conditions of applied load, tire inflation pressure, vehicle speed, rolling condition, and slip ratio, Figure 1-2. The contact stresses are tabulated in such a way that can be used as load boundary conditions for any FE pavement model.
- Pavement industry is specifically interested in having realistic tire contact stresses at different accelerating, braking and cornering scenarios because the design and prediction of pavement response at the road intersections is so crucial. Therefore, special attention was paid in this study for predicting the tire-induced contact stresses on pavements under these conditions.
- The tabulated database was incorporated into the PUI to automatically produce FE input model with realistic non-uniform 3-D loading boundary conditions for PANDA. A sample of the modifications in PUI and the input model can be seen in Figure 1-3.

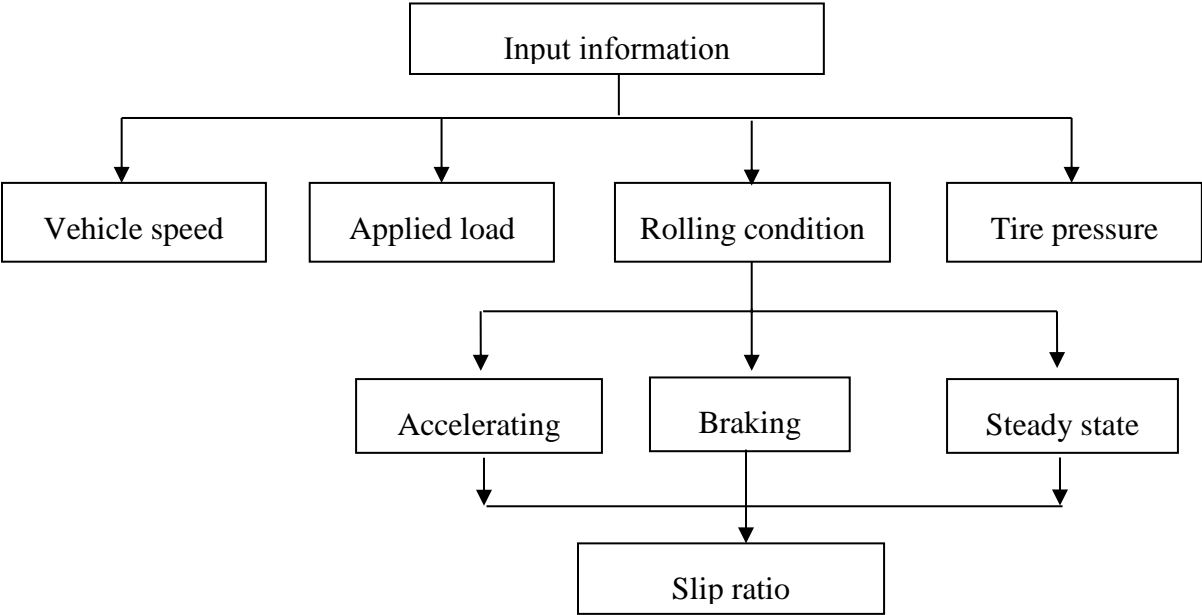


Figure 1-2. The matrix of conducted FE simulations to produce tire-induced contact stresses on the pavement under various conditions.

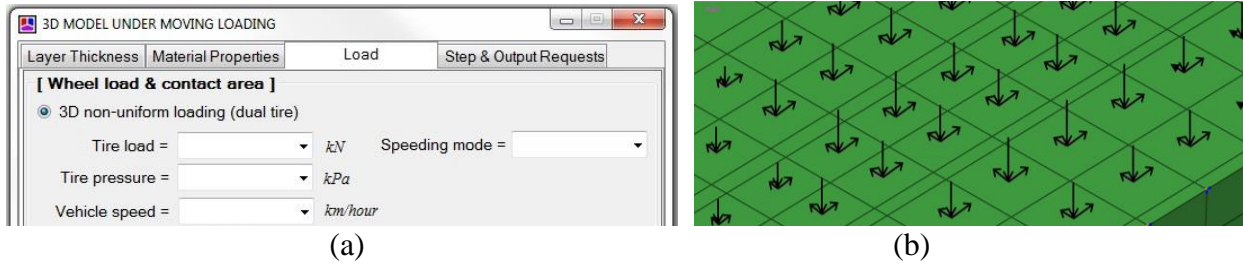


Figure 1-3. A sample representation of (a) revised PUI and (b) a generated FE input file with modified elements width and applied non-uniform 3-D contact stresses.

2 CONTACT STRESS MEASUREMENTS

2.1 MEASURING EQUIPMENT AND EXPERIMENTAL PROGRAM

Distribution of 3-D contact stresses/forces were measured for a dual-tire assembly 275/80R22.5 for a wide range of load ($P=26.6, 35.6, 44.4, 62.1, \text{ and } 79.9 \text{ kN}$) and tire inflation pressure ($\sigma_o=512, 690, 758, 862 \text{ kPa}$). The measurements were performed at the CSIR using SIM Mk IV with the load applied by a heavy vehicle simulator (HVS). The position of the tire in the transverse direction was not changed during testing, so that the pins measured the contact forces at the same location with respect to the tire. The average tire speed was 0.331 m/s and the sampling frequency was 1001 Hz, Figure 2-1.



Figure 2-1. Measuring system and tested tire.

Each measuring pad of the dual SIM Mk IV is 840-mm-long and 471-mm-wide, and it consists of approximately 1040 supporting pins, 21 of each are instrumented with strain gauges. The strain gauges were calibrated to convert the strain to force, which are divided by a geometric factor to obtain stresses. The geometric factor assumes that the tire has no grooves (smooth tire) and is equal to 250.28 mm^2 . The pins are fixed to a 45-mm-thick rigid steel plate and its height is 50 mm.

Every combination of applied load and tire inflation pressure was repeated ten times, and the best three replicates were selected for analysis. Best replicates were identified as the ones where the vertical reaction calculated from the measuring pins was close to the applied load. The measurements were filtered using the moving average methods with a window size of 20 data points. Figure 2-2 demonstrates the three best replicates and the filtered obtained from them. It was observed that the data slightly shifted, but the peak values and the contact length did not change by the filtering process.

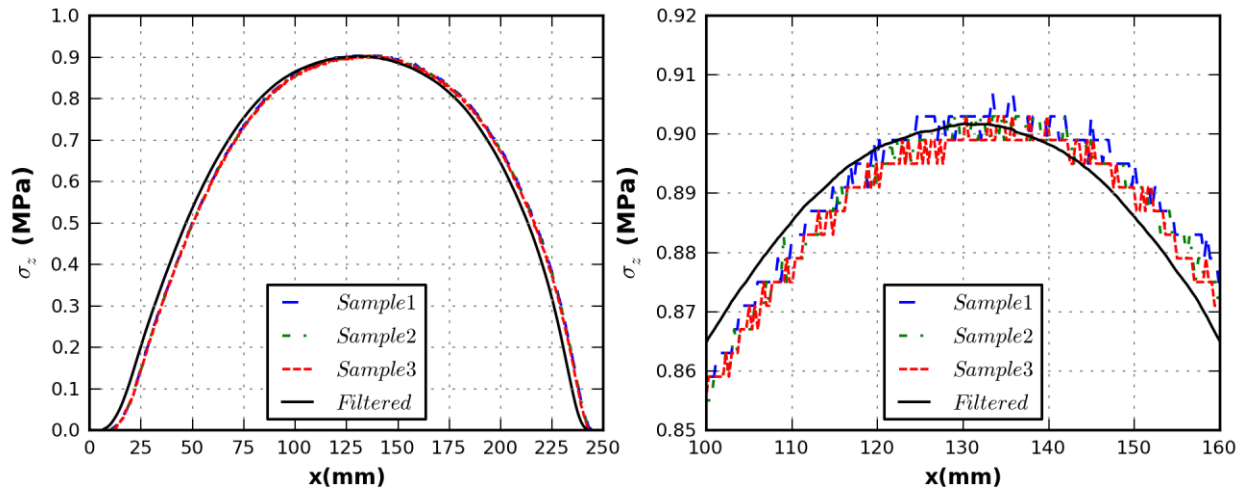


Figure 2-2. Three best replicates and detail of filter process outcome.

2.2 THREE-DIMENSIONAL CONTACT STRESSES

The typical variation of contact stresses in each direction is presented in Figure 2-3. The shape of stress data in the transverse (σ_y) and vertical (σ_z) direction were similar, but they differed in magnitude. For the majority of the load combinations, σ_y and σ_z were zero at the beginning and end of the contact. For a few cases, the transverse contact stresses showed a small negative peak at the rear portion of the tire.

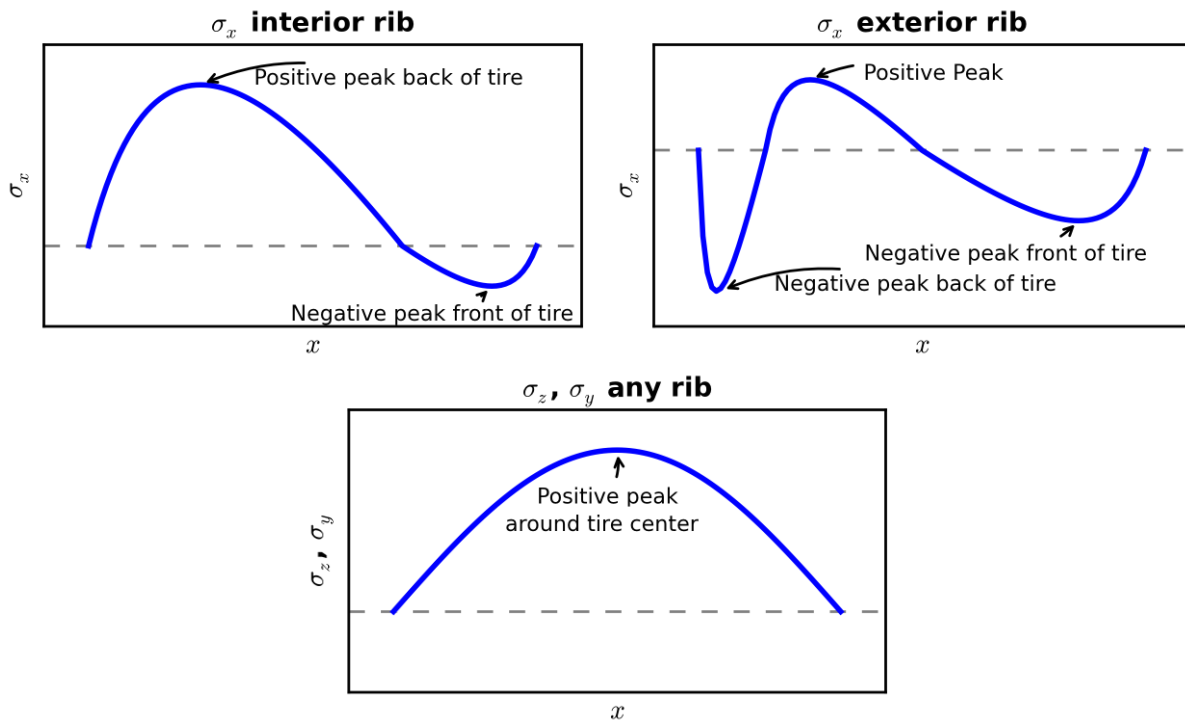


Figure 2-3. Typical variation of 3-D contact stresses along the contact length (σ_x represents longitudinal, σ_y transverse, and σ_z vertical contact stresses).

In the case of longitudinal contact stresses (σ_x), the shapes were dependent on the location of the rib. σ_x had three peaks, two negative and one positive, when the rib was at the edge of the tire. The magnitude of the peak at the rear end of the tire was higher than the one at the front. Conversely, the magnitude of the negative peak at the front of the tire and the positive peak were similar. On the other hand, two extreme values were observed, one positive and one negative, when the rib was located at the interior of the tire, with the positive peak having higher magnitude.

Figure 2-4 illustrates variation of the maximum vertical contact stresses across the DTA for various tire inflation pressure. As expected, if the applied tire inflation pressure, σ_o , increased, the magnitude of the $\sigma_{z,max}$ increased. In addition, *n*-shape pattern, low stress values at the edge of the tire, was seen at low load. As the load increased, the edges of the tire carried more load, and the *n*-shape pattern vanished. It was also noticed that the maximum vertical contact stress is significantly higher than the corresponding tire inflation pressure.

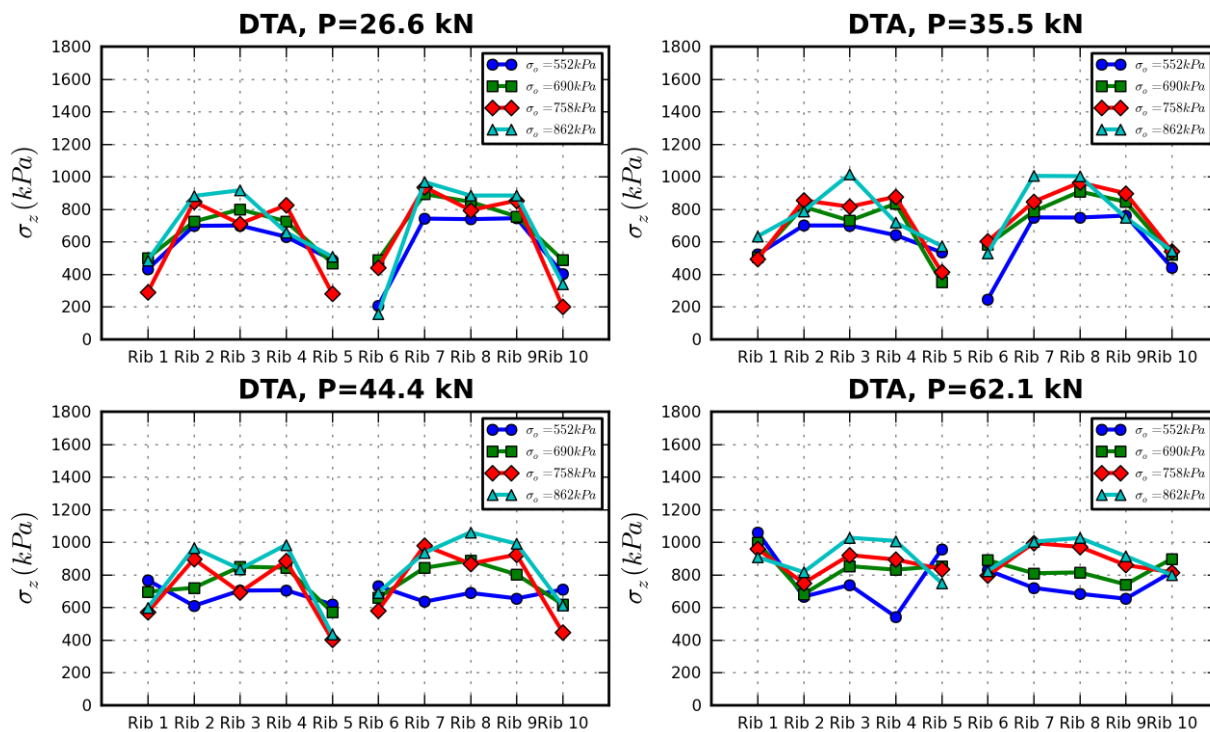


Figure 2-4. Variation of maximum vertical contact stresses, $\sigma_{z,max}$, across tire under different applied load, P .

Figure 2-5 presents the ratio of the maximum transverse contact stress with respect to the vertical one. The plot is presented in normalized form, meaning that all values are divided by the tire inflation pressure. Most data points fall between the $0.1\sigma_z$ and $0.4\sigma_z$ line, indicating that the magnitude of the peak transverse contact stresses can be as high as 40% of the vertical ones. Similar plots are provided in Figure 2-6, where it can be observed that the peak values for longitudinal contact stresses are also relevant, and can be as high as 35% of the vertical contact stresses.

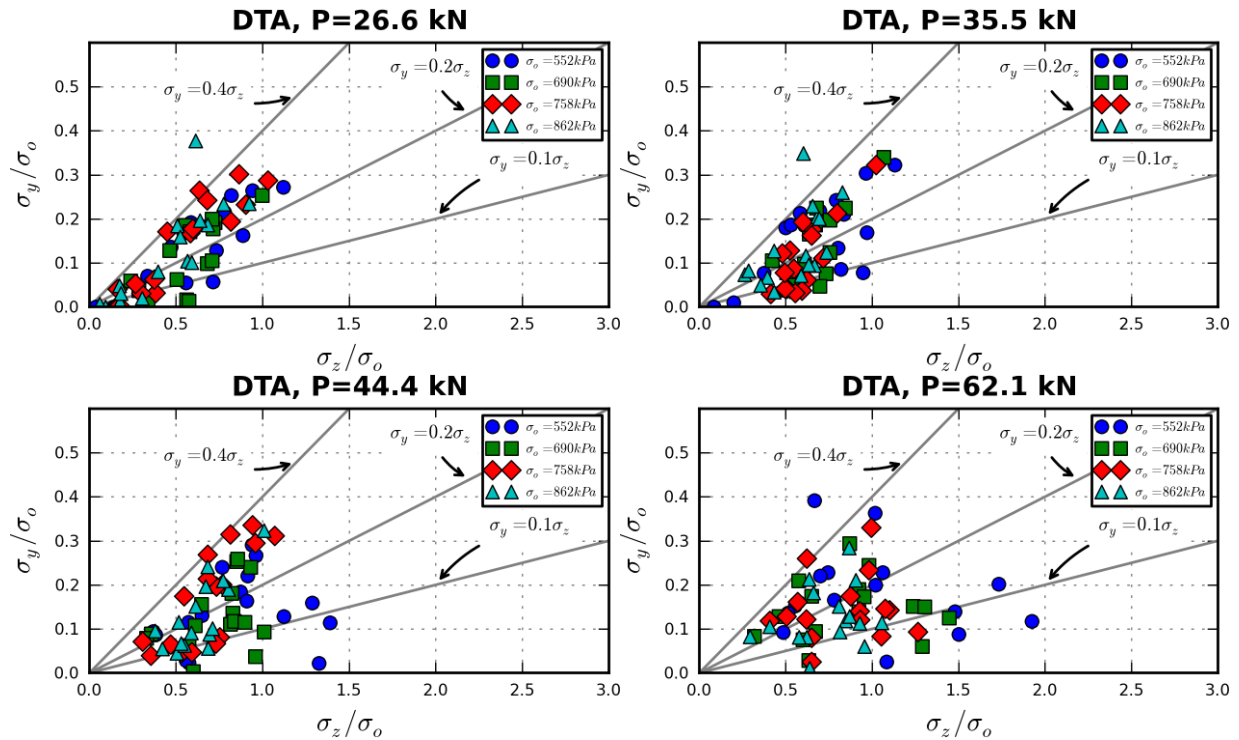


Figure 2-5. Magnitude of normalized maximum transverse contact stress, $\sigma_{y,max}$, with respect to maximum normalized vertical contact stress, $\sigma_{z,max}$.

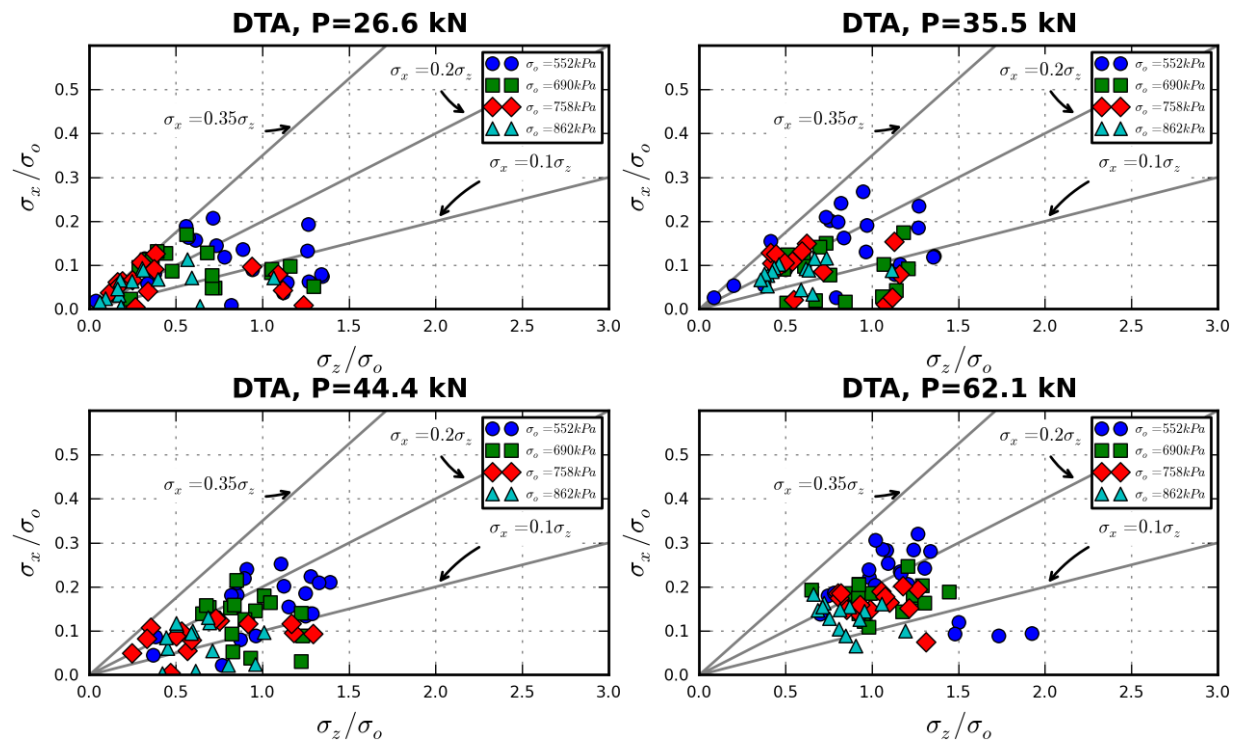


Figure 2-6. Magnitude of normalized maximum longitudinal contact stress, $\sigma_{x,max}$, with respect to maximum normalized vertical contact stress, $\sigma_{z,max}$.

2.3 CONTACT AREA AND LOAD-DEFLECTION CURVES

The contact area was measured by loading the painted tire against white paper. The imprint was scanned and scaled into AutoCAD to properly obtain the contact area. The load-deflection curves were also measured for model calibration. Figure 2-7(a)-(b) illustrates the variation of the contact area and the load-deflection curves, respectively. As the applied load became higher, the slope of each line increased, indicating that the contact area is more sensitive to changes in tire inflation pressure at higher values of applied load. As expected, as σ_o was increased, A_c decreased, and as P approach 79.9 kN, the contact area got higher.

The load-deflection curves are not an indicator of the tire's stiffness (relevant to phenomena such as fuel consumption), but it is also relevant for calibration and validation of the tire model. Figure 2-7(b) shows that the tire stiffness, represented by the slope of each curve, increased as tire inflation pressure increased.

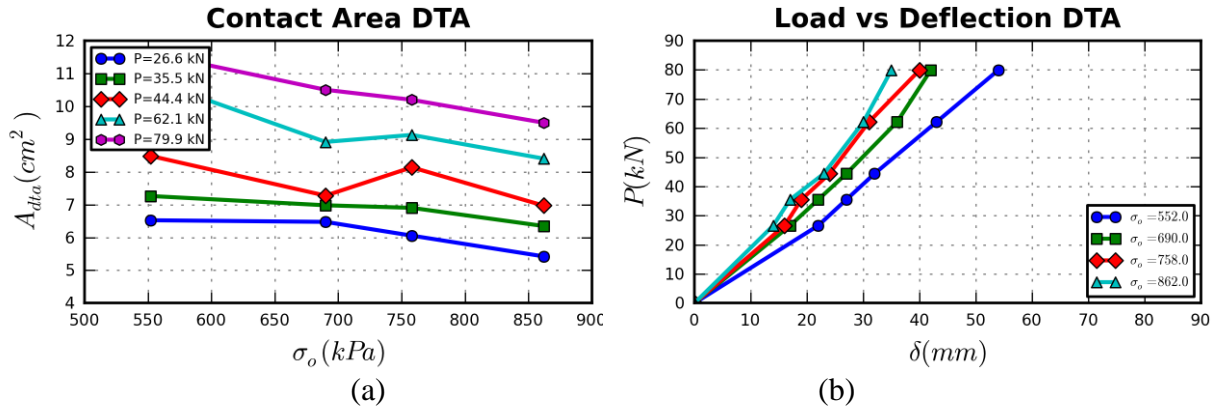


Figure 2-7. Contact area and load-deflection curves.

3 NUMERICAL MODELING

3.1 MODELING APPROACH

Steady-state transport analysis procedure of ABAQUS was used to create the FE model of the tire and predict contact stresses at the tire-pavement interface. This approach is based on the arbitrary Lagrangian-Eulerian (ALE) formulation, which converts a dynamic problem into one where all derivatives are obtained with respect to space variables and allows mesh refinement in selected regions of the model. ALE establishes three domains: i) material domain, which moves with the material; ii) spatial domain, which represents the current configuration; and iii) reference domain, which describes mesh motion.

The analysis of the rolling tire was divided into three stages. First, the axisymmetric model, where the tire's cross-section subjected to the tire inflation pressure was analyzed assuming axisymmetric tire, as shown in Figure 3-1(a). Second, the axisymmetric model was revolved with respect to the transverse axis to create the full 3-D model, as shown in Figure 3-1(b). Finally, rolling analysis of the tire was performed. Figure 3-1 shows the two initial stages. Tire inflation pressure was applied in the axisymmetric model along with the boundary conditions at the tire-rim contact and the axis of symmetry. In the 3-D model, the axisymmetric model is brought to equilibrium, initial contact between the tire and the rolling surface was established, and the load was applied. After that, the rolling analysis was performed, and contact stresses at various conditions, between full braking and full rolling, were calculated.

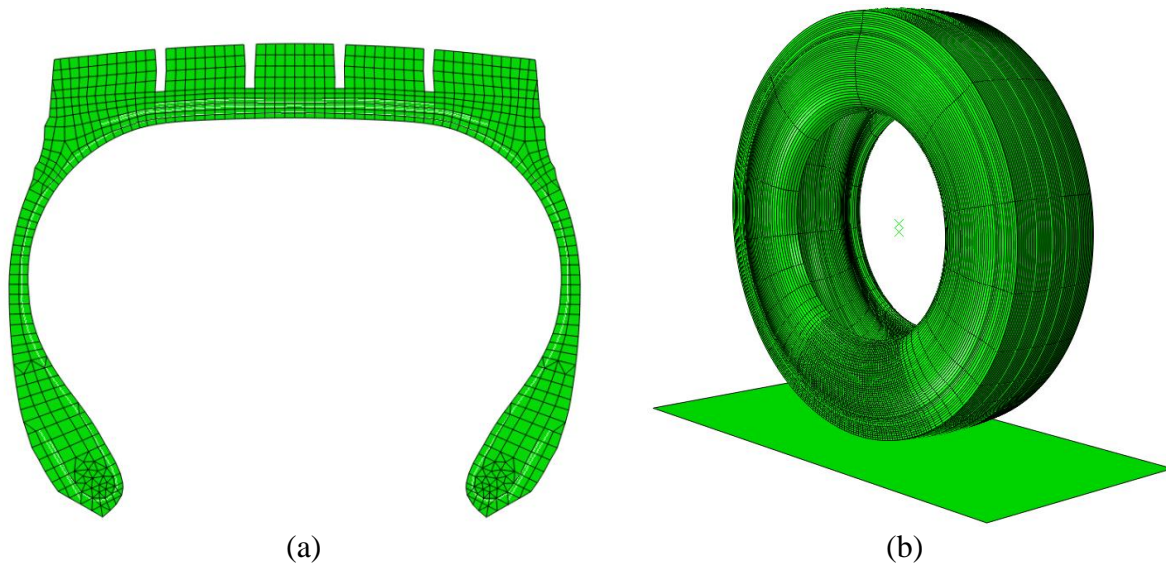


Figure 3-1. Analysis stages.

The complex nature of the tire structure requires special FE elements such as cylindrical, hybrid, and rebar elements. Cylindrical elements exactly represent curve geometries with fewer elements than Cartesian ones, making them ideal for tire modeling. Cartesian and cylindrical elements were combined to obtain accurate contact stresses at the tire-pavement surface contact. Cartesian element were limited to the potential area of contact and the remainder of the tire circumference

was minimized using biased cylindrical elements. The extent of the regions occupied by each type of element was defined in the mesh sensitivity analysis, detailed in subsection 3.4. Moreover, hybrid elements, which incorporate pressure as an independent unknown variable in the constitutive equations, are ideal to model the incompressibility of rubber and were therefore used in this study. Finally, rebar elements were incorporated in the tire FE model to represent the reinforcement of the tire structure. These type of elements considers rubber and reinforcement independently, therefore laboratory-determined material properties for these tire components could be adequately included in the model without homogenization.

Friction is a relevant factor when predicting contact stresses. As a consequence, an appropriate velocity-dependent friction model was adopted (Wang, 2013). Figure 3-2 presents the variation of friction coefficient with speed for three macro-texture: good, poor, and intermediate. The contact stresses presented in this research were calculated using intermediate surface texture.

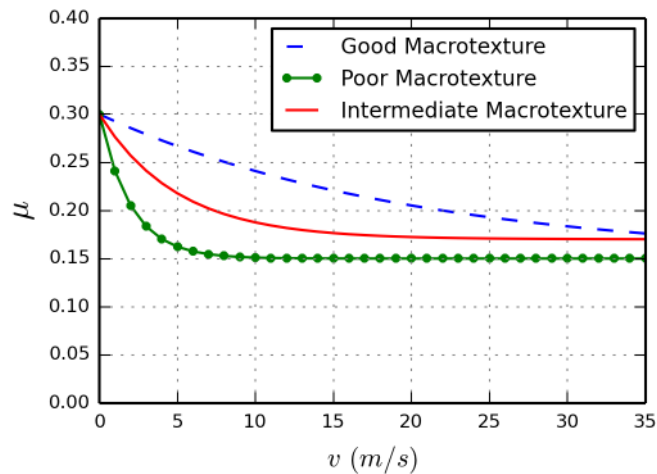


Figure 3-2. Friction coefficient vs. vehicle velocity based on Wang (2013) friction model.

3.2 GEOMETRY OF THE FINITE ELEMENT MODEL

DTA 275/80R22.5 was considered in this study. The tire's nomenclature indicates that the tire is 275-mm wide, the ratio between the tire's height and width is 80%, and that the diameter of the rim is 22.5 in. Based on this information, it can be inferred that the tire has a radius of 505.7 mm. The outside perimeter of the tire, from heel to heel, is 686.3 mm. This value does not include the distance inside the grooves. The inside perimeter, from toe to toe excluding the distance inside the grooves, is 686.3 mm. The tire consists of three belts, each with a specific reinforcement orientation and width as presented in Table 3-1. The belt closest to the tire's interior is labeled Belt 1, while the one closest to the tread is named Belt 3. Table 3-1 also shows the number of reinforcement cords in 10 mm; this information was used to infer the reinforcement's spacing. All belts are hosted by the belt packaged, which has a thickness of 6.4 mm.

Table 3-1. Reinforcements details.

Reinforcement	Width (mm)	Orientation (°)	Spacing (Cords/10 mm)	Area (mm²)
Belt 1	201.9	113.0	37	1.370
Belt 2	180.1	73.0	41	1.370
Belt 3	137.2	73.0	33	1.704
Ply		1.0	31	1.167

The thickness of the inner liner, which is the inner-most component of the tire, is 2.1 mm. In addition, the thickness between the inner liner and the belt package (body ply thickness) is 3.0 mm. The thickness of the tread in the middle of the tire is 26.1 mm. Adding the thicknesses of the inner liner, body ply, belt package, and tread would result into the total crown thickness (37.5 mm). The total shoulder thickness is the distance from the corner of the outer tread to the inner surface of the tire measured perpendicular, and it is 37.9 mm. The thickness of the sidewall is 10.31 mm. The tire's bead consists of a rectangular array of wires (8x6), each 2.0 mm wide and 1.3 mm long, as shown in Figure 3-3.

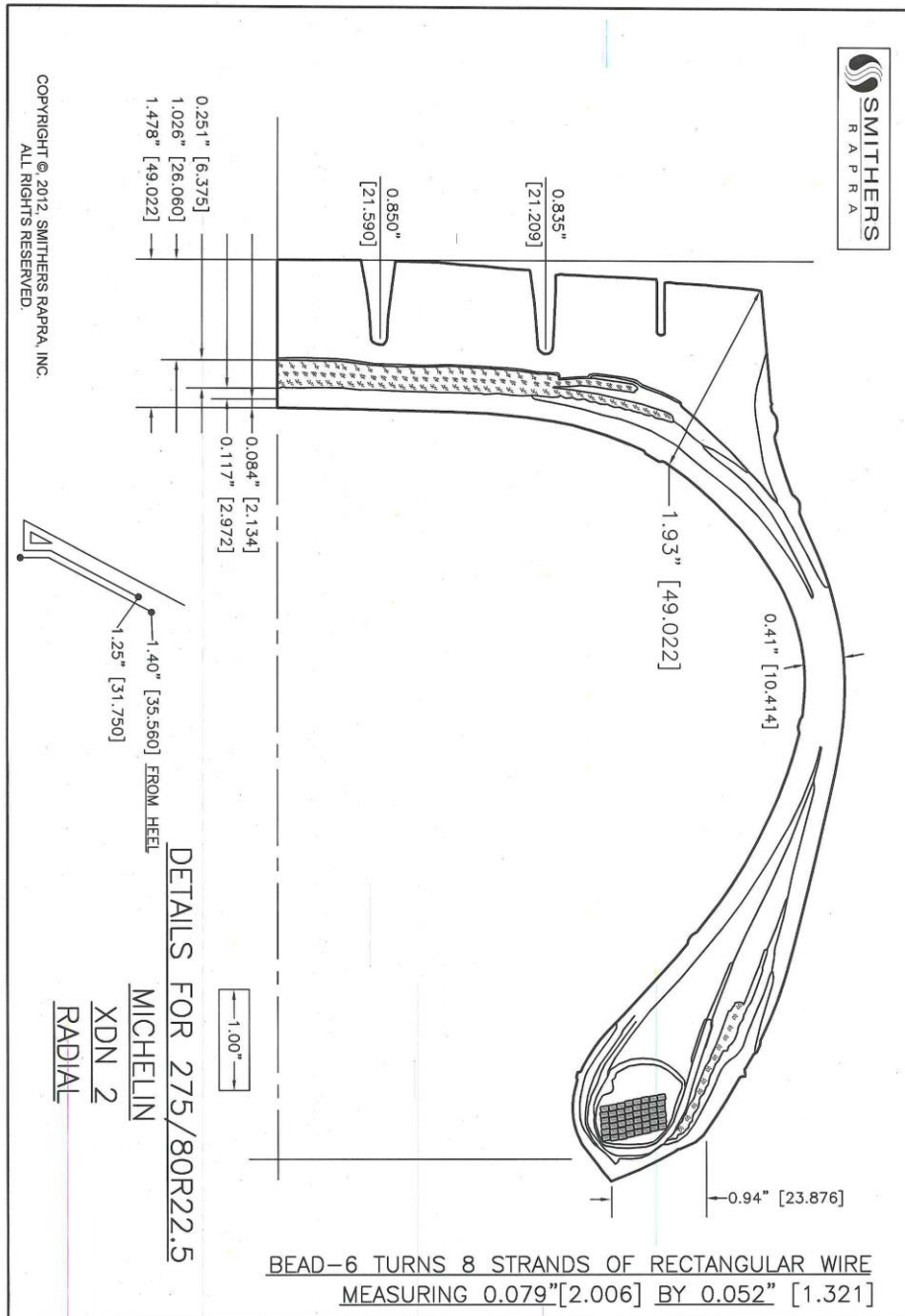


Figure 3-3. Tire's (DTA 275/80R22.5) dimension in the cross section.

3.3 CHARACTERIZATION OF TIRE MATERIALS

Two material constitutive models were used to simulate the tire: linear elastic for reinforcement (ply and belts) and hyperelastic for rubber. The reinforcements mainly consist of materials that can be properly represented by elastic modulus and Poisson's ratio. However, rubber components

experience large deformation as the magnitude of the applied load increases. Consequently, the linear elastic model is not suitable and hyperelasticity becomes a better choice.

The elastic modulus of the reinforcement was determined following ASTM D882. During the test, the reinforcement was properly clamped, and tensile load was applied to obtain the stress-strain curve. Five samples were tested from each material; a typical stress-strain curve is shown in Figure 3-4. A portion with a very low slope, caused by the initial setting of the load, as noticed at the beginning of the curve, was discarded during calculation of the elastic modulus. This figure also illustrates the average of the elastic modulus of the samples.

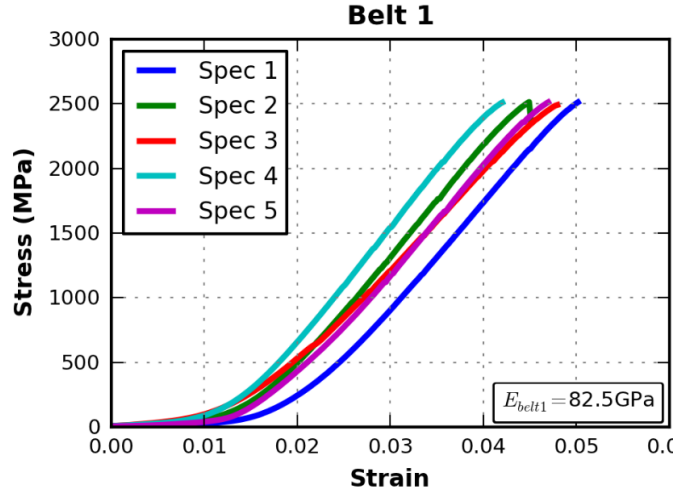


Figure 3-4. Stress-strain curve for Belt 1.

Mooney-Rivlin behavior was adopted for rubber. In this model, the variation of strain energy with the principal invariants of Cauchy-Green deformation tensor is given by:

$$W = C_{10}(I_1 - 3) + C_{01}(I_2 - 3) \tag{1}$$

Where: W =strain energy density;

I_1 and I_2 = first and second principal invariants of the right Cauchy-Green deformation tensor; and

C_{01} and C_{10} =empirically determined constants.

The material constants C_{01} and C_{10} were provide by the tire manufacturer and are presented in Table 3-2.

Table 3-2. Mooney-Rivlin constants for rubber components

Component	C_{10} (MPa)	C_{01} (MPa)
Tread	0.9753	0.0
Shoulder	0.9763	0.0
Sidewall	0.5479	0.0
Bead filler	0.6034	0.0

3.4 OPTIMIZED MESH FOR THE FINITE ELEMENT MODEL

Total strain energy, which is minimized by the FE method, was used as a criterion to define the optimum mesh configuration. The optimized mesh was defined as the one with the least amount of elements that kept the value of the total strain energy accurate. The “exact” value of the total strain energy was assumed to be given by a mesh with very small elements. For the axisymmetric model, the mesh configuration presented in Figure 3-5 was analyzed. The assumed symmetry of the DTA cross-section was exploited and only half of the cross-section was evaluated to reduce computational effort, while still meeting the desired accuracy. The total strain energy as function of the number of elements is plotted in Figure 3-6.

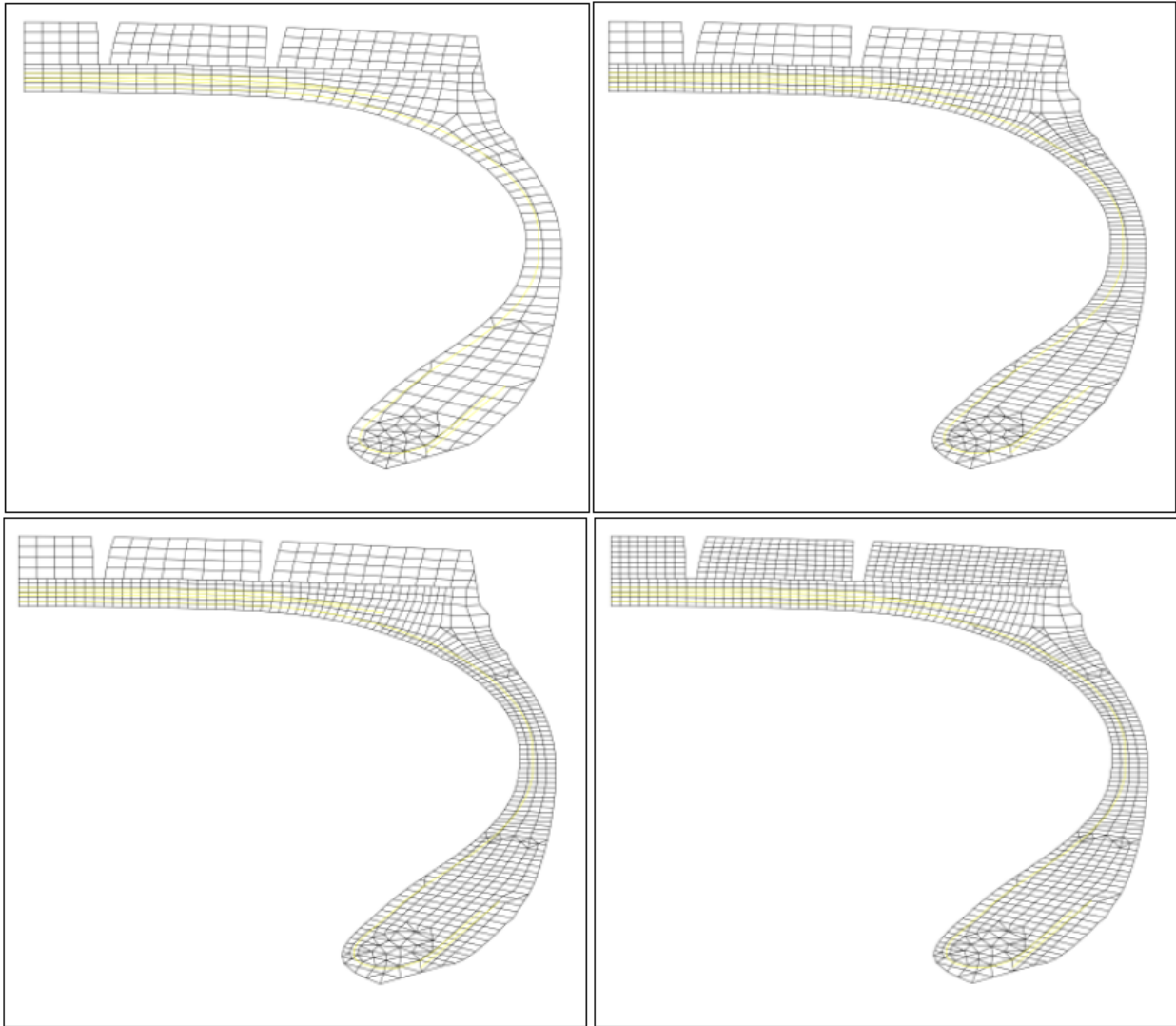


Figure 3-5. Mesh configuration considered in the half-axisymmetric model.

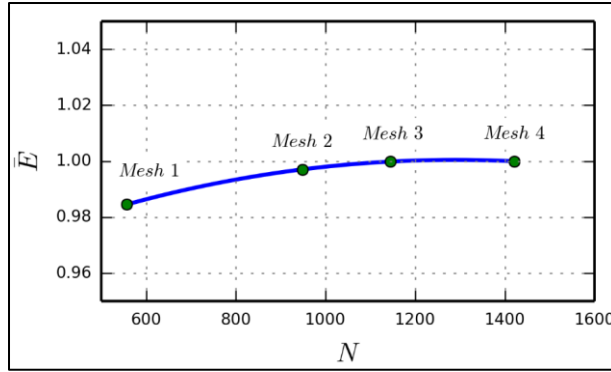


Figure 3-6. Variation of normalized total strain energy, E , with number of elements, N .

It should be noted that additional configurations were studied, and factors such as excessive distortion, geometric constraints, and element type were analyzed. From Figure 3-6, it can be concluded that Mesh 1 does not provide accurate results and that the normalized strain energy is close to the finest mesh. However, the amount of element in Mesh 3 is close to the mesh with the lowest amount of elements. Mesh 2 proved to be the optimum mesh: the ratio between its total strain energy and the one for the finest mesh is higher than 0.98, and the number of elements is minimum. Mesh 2 was selected as the configuration of the half-axisymmetric model.

The same approach was followed to define the element size and distribution in the half tire model. First, two regions were defined: i) the Foot is the region on potential contact area with the surface which is spanned 60° ; and ii) the region with cylindrical elements. First, the amount of elements in the Foot was set to 60, and the size and bias factor of the cylindrical elements was changed to 10, 20, 40, 60, 70, and 80 elements. Second, after defining the distribution of cylindrical elements, the number of elements in the Foot varied: 20, 30, 60, 120, and 240. The variation of the normalized total strain energy with respect to the number of elements in the two regions described above is presented in Figure 3-7. It is observed that there is no relevant influence of the number of elements in the strain energy values. The selected mesh configuration was 60 elements in the Foot, and 20 cylindrical elements, 10 at each side of the Foot.

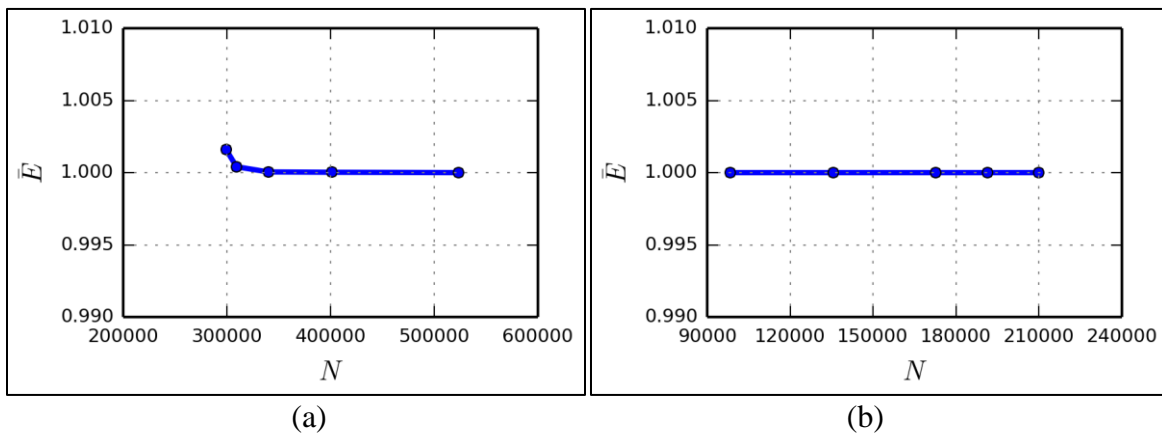


Figure 3-7. Variation of normalized total strain energy with number of elements along the (a) foot and (b) region with cylindrical elements.

3.5 CALIBRATION AND VALIDATION OF NUMERICAL MODEL

Calibration of the FE model was based on the contact area, A_c , and deflection, δ , when the tire was subjected to a load of $P=44.4$ kN and a tire inflation pressure of $\sigma_0=690$ kPa. After reasonable match was reached between predicted and calibrated results, the material properties were fixed, and the FE model was simulated for the combination of load and tire inflation pressure ($P=26.7$, 35.6, and 44.4 kN, and $\sigma_0=552$, 690, and 758 kPa) and contact area, deflection, and maximum vertical contact stresses were compared.

In order to group the results in a single value, the mean absolute percentage error (*MAPE*) was adopted. *MAPE* is given by:

$$MAPE = \frac{100}{n} \sum_{i=1}^n \left| \frac{Meas_i - Calc_i}{Meas_i} \right| \quad (2)$$

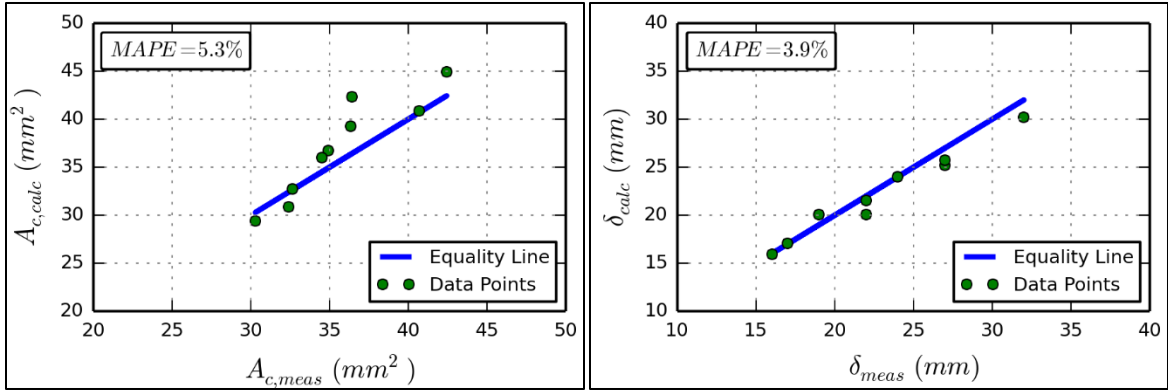
Where: n =number of measurements;

$Meas_i$ =measurement i , corresponding to a combination of P and σ_0 ; and

$Calc_i$ =calculated value i , corresponding to the same combination of P and σ_0 as in $Meas_i$.

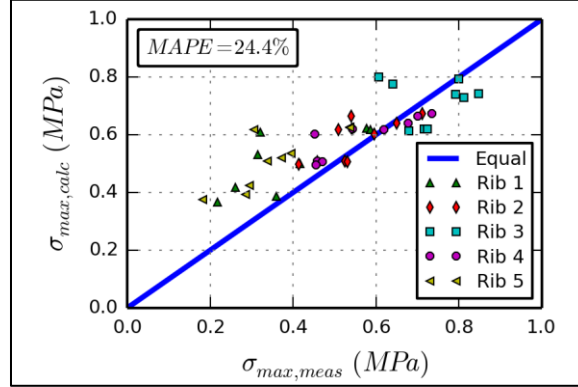
Figure 3-8 compares the experimentally measured and FE calculated deflection and contact area, and maximum vertical contact stresses. For the maximum vertical contact stresses, a free rolling analysis at low speed was performed (see chapter 4) using high friction coefficient. For contact area and deflection, the static model was used. These two approaches better represent the conditions used during the experimental measurements.

As shown in Figure 3-8, a very good agreement between measured and calculated contact area and deflection was obtained ($MAPE = 5.3$ and 3.9% , respectively). However, the match of maximum vertical contact stresses is not as good ($MAPE = 24.4\%$). The best agreement was observed for the central ribs, which were used to control the position of the tire as it rolls over the dual SIM system. This agreement is due to the great sensitivity of the contact stresses measurement to the position of the tire with respect to the measuring pins.



(a)

(b)



(c)

Figure 3-8. Measured vs. calculated (a) contact area, (b) deflection, and (c) maximum contact stresses.

4 ANALYSIS OF CONTACT STRESSES

Tire-pavement contact stresses are governed by the loading conditions, tire characteristics, and rolling scenarios. A full factorial of the DTA simulations on an infinitely rigid surface was completed, by which the main factors include the applied load P , tire inflation pressure σ_0 , rolling speed V , slip ratio $s_{b/t}$, and slip angle θ , Figure 4-1. In addition, the three steady-state rolling scenarios considered were accelerating, braking, and cornering, wherein each mode resulted to varying implications on the contact stresses. A brief overview of each scenario is provided in proceeding section.

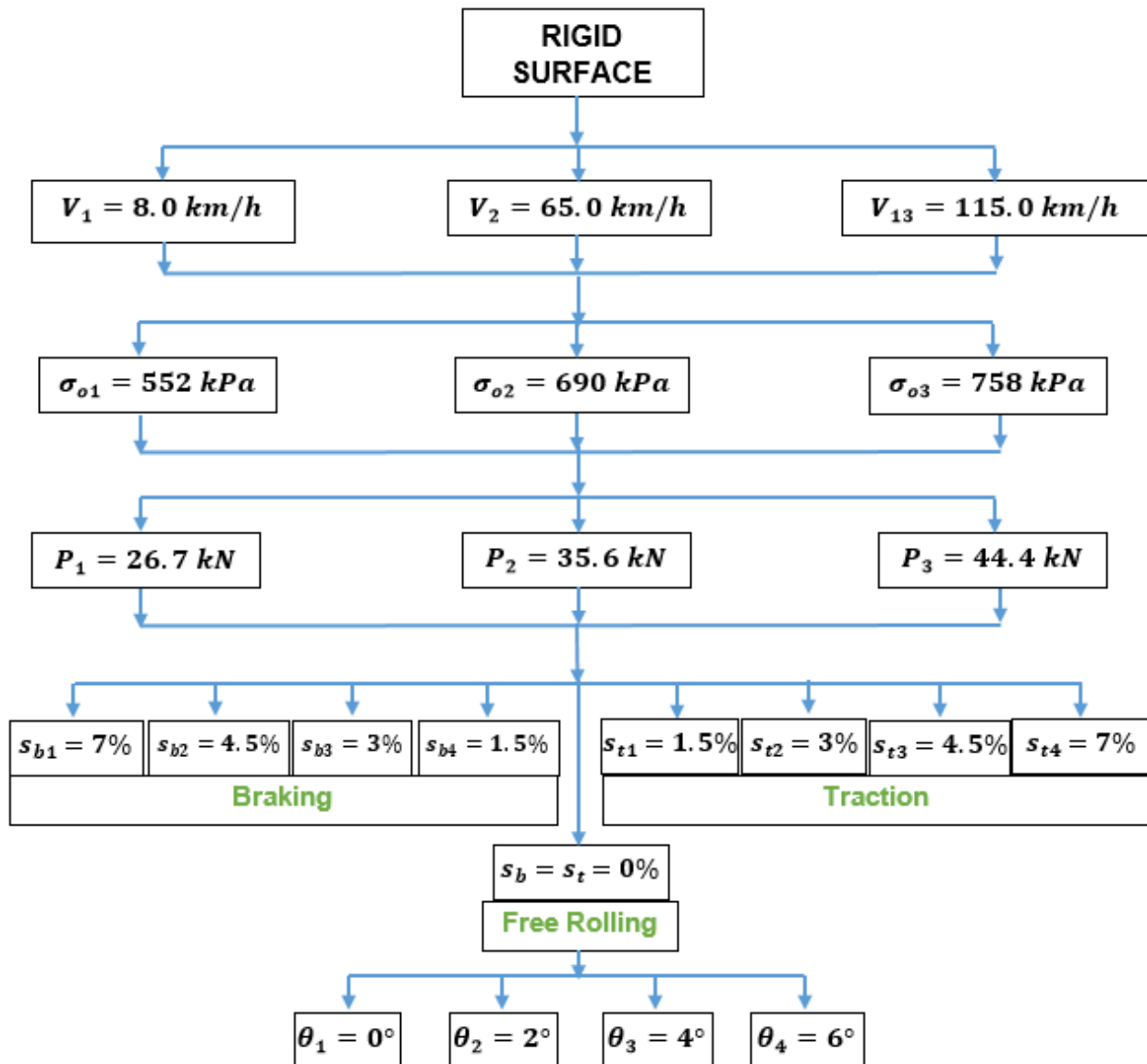


Figure 4-1. Analysis matrix of the DTA simulations on a rigid surface.

For acceleration, a driving torque is applied about the axis of rotation of the tire, thereby producing a tractive force; whereas a braking torque generates a force to decelerate the tire. In addition,

another indicator of differentiating acceleration versus deceleration are the directions of the torque and the angular velocity. Given that the torque and angular velocity are moving clockwise (towards the direction of the translational speed), then this scenario is characterized as accelerating. On the other hand, when the applied torque is moving counter-clockwise and the angular speed tends to the opposite direction, then the tire is experiencing a braking condition.

As tractive force at the tire-pavement contact area is developed during acceleration, not only does the tire tread at the front of the tire experience compression but a corresponding shear deformation of the sidewall is also developed (Wong, 2008). The compression of the tread elements before entering the contact area reduces the distance that the tire traverses in comparison to a free-rolling condition. This is a phenomenon often referred to as “longitudinal slip.” According to the Society of Automotive Engineers (SAE), longitudinal slip is the ratio between the longitudinal slip velocity and the spin velocity of the straight free-rolling tire, expressed in percentage. Therefore, the slip ratio at traction, s_t , is defined as:

$$s_t = \left(\frac{r\omega}{V} - 1 \right) * 100 = \left(\frac{r}{r_e} - 1 \right) * 100 \quad (4.1)$$

where r is the rolling radius of the free-rolling tire, ω is the angular speed, V is the linear speed, and r_e is the effective rolling tire radius, which is the ratio between the linear and angular speeds of the tire.

In contrast to acceleration, when a braking torque is applied, tread elements are stretched prior to entering the contact area, which indicates that the distance that the tire will traverse is greater than that of the free-rolling scenario. The slip ratio for the braking condition, s_b , is defined as:

$$s_b = \left(1 - \frac{r\omega}{V} \right) * 100 = \left(1 - \frac{r}{r_e} \right) * 100 \quad (4.2)$$

The third rolling condition is cornering. This scenario occurs when a tire is subjected to a force perpendicular to the translational travel direction. A lateral or “cornering” force is then developed as the tire travels along a path at a given angle with the wheel plane, also called as the “slip angle.” Generally, the slip angle impacts the tire’s directional control and stability (Wong, 2008). In order to impose a slip angle, θ , the linear speed is used to generate velocities in the longitudinal and transverse directions, using the following equations.

$$v_x = V \cos \theta \quad (4.3)$$

$$v_y = V \sin \theta \quad (4.4)$$

where v_x and v_y are the longitudinal and transverse velocities, respectively.

Prior to delving into the details of the contact stress analysis, it is only suitable to define the free-rolling condition of the tire. After the initial start of rotating the tire, there is a corresponding angular speed wherein the driving torque is zero – generating a “free-rolling” tire. For this study, the free-rolling condition was used as a baseline to compare the remainder of the simulation matrix. In its physical nature, as the tread enters and traverses along the contact area, the distance from the center of the wheel varies from the unloaded radius to the loaded radius. This phenomenon generates a negative shear stress at the front part of the tire as its speed reduces upon entering

(recall the local compression of the tread), and results to a positive shear stress at the trailing edge due to the tread stretch upon its exit (Pauwelussen, 2015).

The typical variations in the three orthogonal directions is shown in Figure 4-2, wherein the loading conditions were held constant with the applied load, $P = 44.4 \text{ kN}$ and tire inflation pressure, $\sigma_0 = 690 \text{ kPa}$; and the translational speeds were varied. Generally, altering the linear velocities did not affect the contact stress distributions along the contact length for a free-rolling tire.

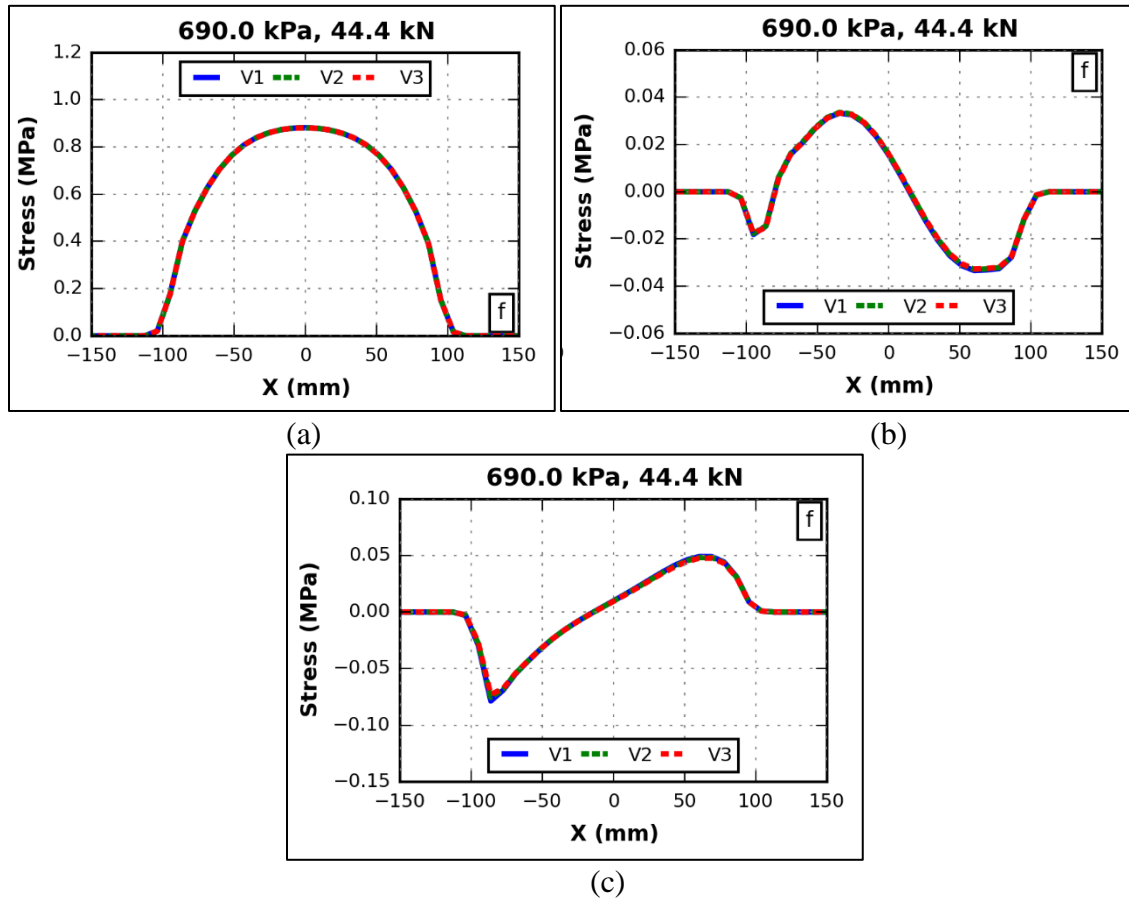


Figure 4-2. Contact stress variation along the contact length of a free-rolling tire varying velocities ($V1 = 8$, $V2 = 65$, $V3 = 115 \text{ km/h}$) in the (a) vertical, (b) longitudinal, (c) transverse directions.

It was also observed that varying the tire inflation pressure changed the maximum vertical contact stress value, $\sigma_{z,max}$, along the fifth meridian at the middle rib (Rib 3). One should note that a meridian is a longitudinal line that runs along the circumference of the tire. Given a constant $P = 26.7 \text{ kN}$, $\sigma_{z,max}$ was estimated to 0.75 MPa when $\sigma_0 = 552 \text{ kPa}$, and resulted to 0.92 MPa when $\sigma_0 = 690 \text{ kPa}$ – indicating an 18% increase. On the other hand, when P was varied from 26.7 kN to 44.4 kN, holding σ_0 constant, the peak value of the vertical stress was not impacted, instead the contact length was increased (Appendix A). Additionally, it is worth noting that with the inherent increase of the applied load, edges of the outer ribs began to carry a significant amount of load in contrast to other locations.

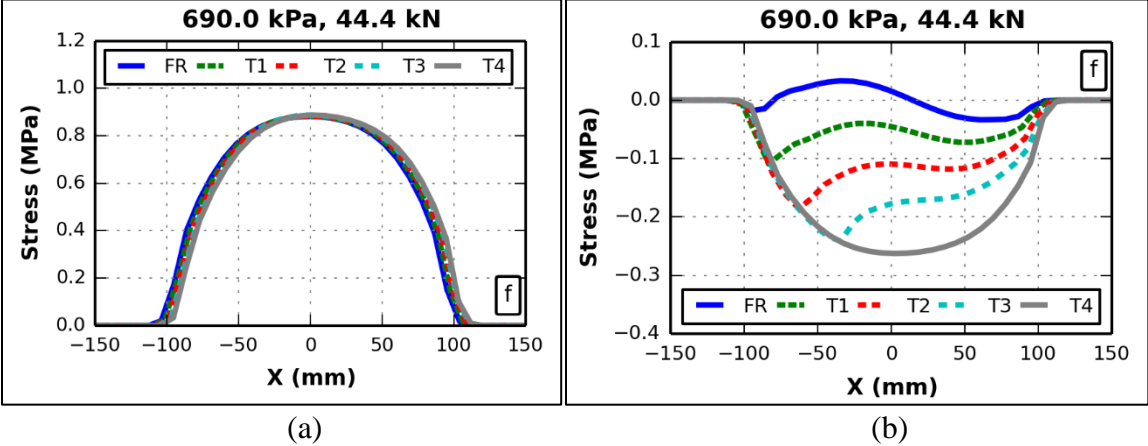
In regard to longitudinal contact stresses along the fifth meridian of Rib 3, for all combinations of P and σ_0 , there were three distinct peaks observed. This behavior was characterized by the variation of the speed directions along the contact length, from the entrance to the exit of the tire treads. Moreover, as the applied load was increased, the magnitude of all the peaks increased, which was apparent when each tire inflation pressure was held constant.

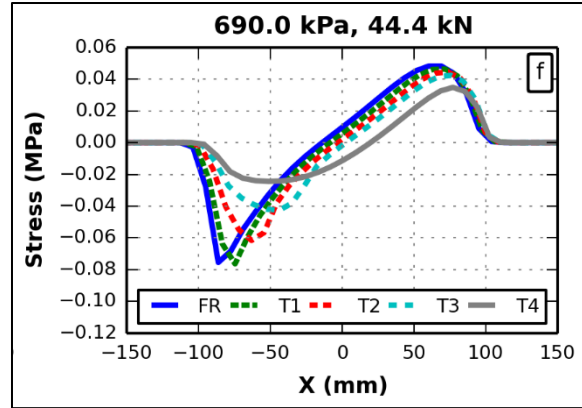
On the contrary, varying σ_0 from 552 to 758 kPa led to an evident decrease of the peak values. Due to the dependence of longitudinal contact stresses on relative tread deformations along the contact length, an increase in the tire inflation constricted the treads to displace, thereby reducing the peak values. And for the same reason, increase in the contact length provided greater freedom for treads to move, which resulted in increase of peak magnitudes.

Lastly, transverse contact stresses are typically generated due to the lateral displacement of the loaded tire treads. One can observe from Appendix A that the local maxima and minima slightly increased when the tire inflation pressure was increased. In addition, although the change in applied loads did not vary the peaks of the transverse contact stresses along the second meridian of Rib 3, there was a small extension of the transverse contact stress distribution along the contact length.

4.1 ACCELARATING SCENARIO

In order to assess the impact of an accelerating tire on contact stresses, the tractive slip ratio, s_t , was varied. The selected values provided a transition from the free-rolling condition with zero torque, to increasing driving torque and angular speeds, until full traction was reached. The values were 1.5%, 3%, 4.5%, and 7%, and were indexed as T1, T2, T3, and T4, respectively on the following plots. Figure 4-3 illustrates typical contact stress variations in the three orthogonal directions, given that $V = 8.0 \text{ km/h}$, $P = 44.4 \text{ kN}$, and $\sigma_0 = 690 \text{ kPa}$. It is also noteworthy that the free-rolling condition is denoted with FR on the figures.





(c)

Figure 4-3. Typical contact stress variation of an accelerating tire with $V = 8 \text{ km/h}$, $P = 44.4 \text{ kN}$, and $\sigma_0 = 690 \text{ kPa}$ in the (a) vertical, (b) longitudinal, and (c) transverse directions.

From the baseline of a free-rolling tire, as traction was increased, vertical contact stresses remained marginally affected by s_t as the curves were nearly coincidental along the contact length with a slight shift to the right, Figure 4-3(a). The same behavior was observed when the velocity was altered from 8 to 115 km/h, wherein the vertical contact stress distributions did not vary (Appendix B).

On the other hand, shear stresses in both longitudinal and lateral directions were more significantly affected. As traction level was increased, the change in sign for the two peaks in the free-rolling tire diminished and higher compressive longitudinal contact stresses along the fifth meridian of Rib 3 were generated, Figure 4-3(b). One can observe that as a 1.5% tractive slip ratio was imposed, the positive peak at the trailing end of the tire changed signs from positive to negative.

As the slip ratio was further increased, higher compressive longitudinal contact stress was generated towards the rear end of the tire at a higher rate than the front. Once full traction was reached at 7%, the distribution assumed a convex shape and the initially-observed multiple peaks along the contact length diminishes. Similar trends were seen for the other cases with increasing velocity (Appendix B). However, a slight increase, past the values under full traction, on the compressive longitudinal contact stress at trailing end was observed as velocity increased up to 115 km/h.

Conversely, the transverse contact stresses along the second meridian of Rib 3 indicated a more subdued change when the traction level was increased. From a free-rolling condition, both peaks from the front and trailing parts showed reductions, wherein the rear end tend to zero more evidently than the values towards the front part of the tire, Figure 4-3(c). This phenomenon could be explained by the reduction of the restricted movement of tread elements against the infinitely rigid surface as the tractive slip ratio was increased. Furthermore, as velocity was increased, a slight reduction of the peaks was also generated (Appendix B).

4.2 BRAKING SCENARIO

The same slip ratio values were applied for the braking conditions. A typical variation of the contact stresses along the representative meridian of Rib 3 is presented in Figure 4-4, given that $V = 8 \text{ km/h}$, $P = 44.4 \text{ kN}$, and $\sigma_0 = 690 \text{ kPa}$. Similar designation with the accelerating condition was used for the braking slip ratios wherein B1, B2, B3, and B4 correspond to 1.5%, 3%, 4.5%, and 7%, respectively. Based on Figure 4-4(a), increasing the braking slip ratio resulted to a slight shift of vertical contact stresses away from the center. However, the overall distribution along the contact length remained relatively the same. On the contrary, the longitudinal and transverse contact stresses were affected differently.

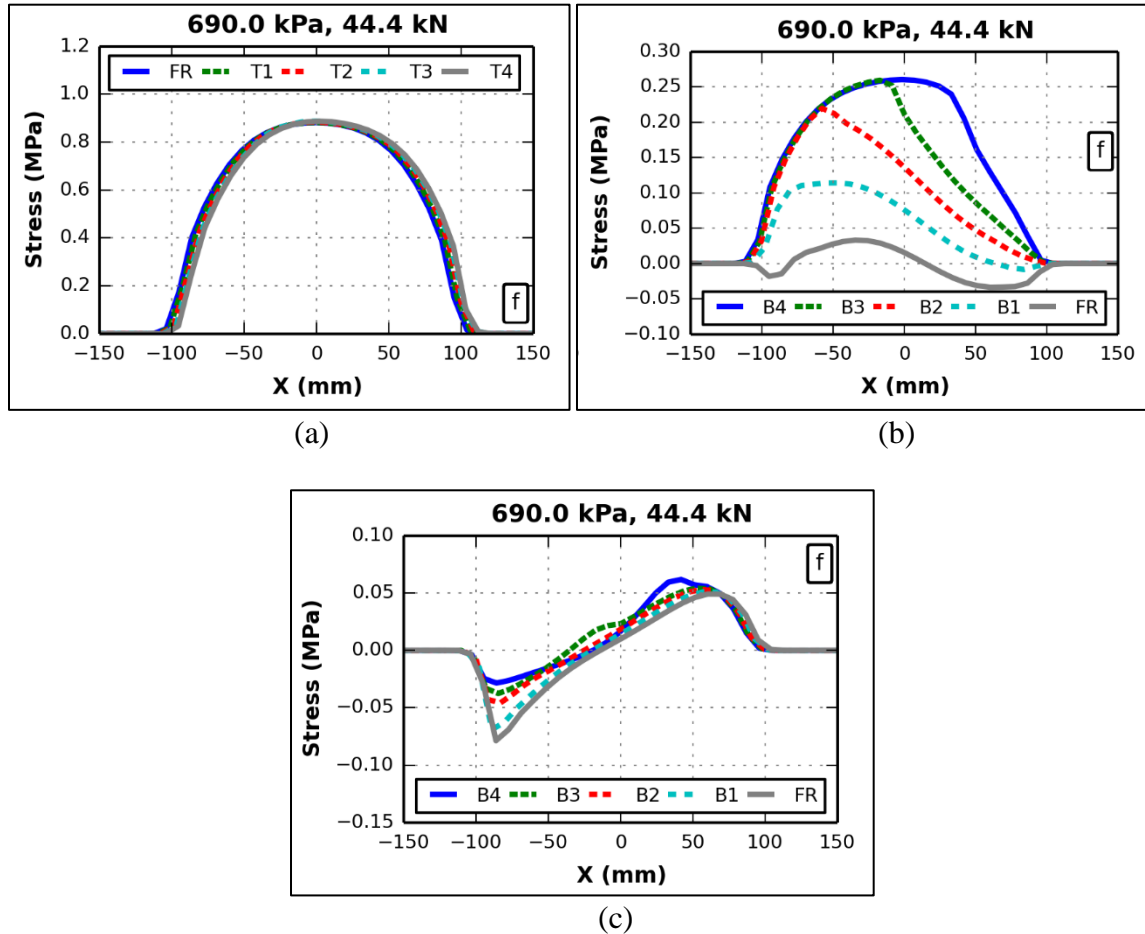


Figure 4-4. Typical contact stress variation of a braking tire with $V = 8 \text{ km/h}$, $P = 44.4 \text{ kN}$, and $\sigma_0 = 690 \text{ kPa}$ in the (a) vertical, (b) longitudinal, and (c) transverse directions.

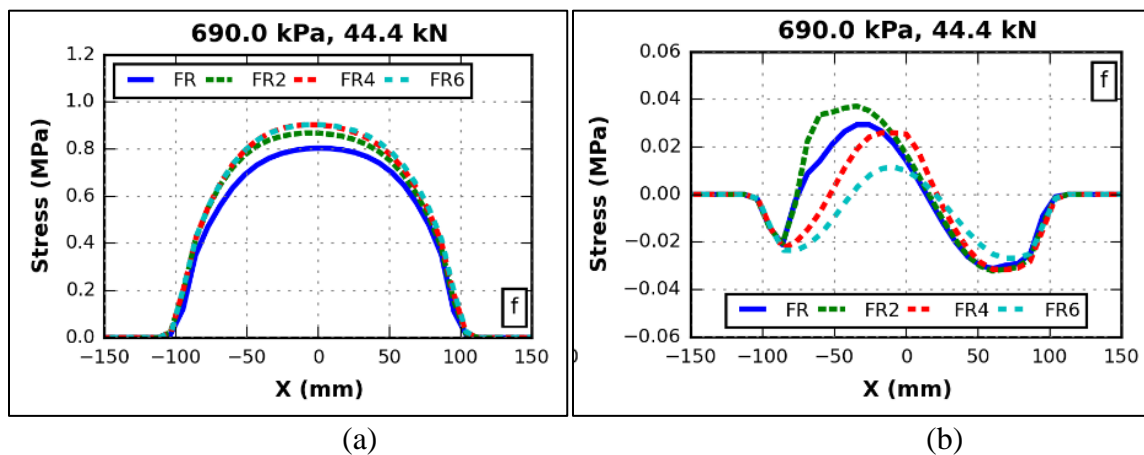
The negative peaks of the longitudinal contact stresses at free-rolling condition diminished and shifted towards the positive values. This change in behavior was more predominant at the trailing part of the tire, wherein one could observe that the positive peak of the free-rolling scenario was pulled closer to the distribution of the full traction case. This indicated that the rear end of the tire was first to reach the limit governed by the friction coefficient. As the braking level was further increased, the longitudinal stress variation from the middle of the contact length on the rear end of tire became coincidental with the full traction values, imposing a further application of the friction limit on the corresponding tire-pavement contact area.

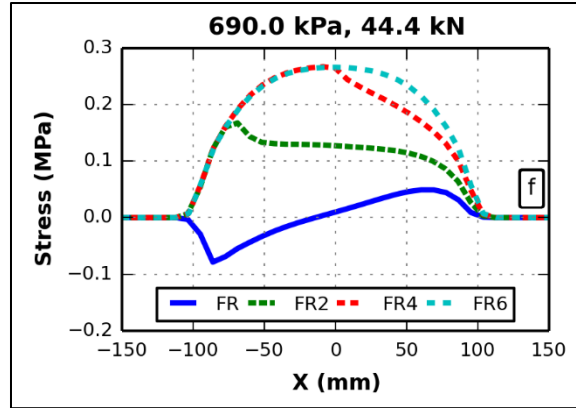
Although the transverse contact stresses showed a slight increase on the positive peak and relative decrease on the negative peak (at the same meridian location as the tractive cases), the impact of the varying brake slip ratios were less significant in comparison to longitudinal contact stresses. This implied that the high increase in longitudinal contact stresses inherently caused the shear stresses to be predominantly oriented in the opposite direction to traffic, thereby reducing transverse contact stresses as slip ratios increased.

Similar to the accelerating scenarios, from Appendix C the variation of linear speed from 8 to 115 *km/h* did not alter the variation of the vertical contact stresses. However, for the longitudinal contact stresses, as the translational velocity increased, the magnitudes across the contact length decreased. This might be attributed to the friction coefficient model assumed, wherein the friction coefficient decreased as the sliding speed increases. This relationship significantly influenced longitudinal contact stresses, and thereby explained the corresponding reduction. Lastly, transverse contact stresses indicated a slight reduction with an increase on the linear speed.

4.3 CORNERING SCENARIO

In a cornering condition, the friction at the tire-pavement interface prevented lateral tread movement, thereby producing lateral deformation. By imposing a slip angle, a lateral force induced a movement away from the rolling direction of the tire. The lateral force also invoked a shift and concentration of contact stresses towards one side of the contact area, which generally coincided with the inner side of the maneuver. One could then imagine that the symmetry of contact stresses along the contact width became asymmetric. In addition, the cornering motion was anticipated to generate in-plane shear stresses that was predominantly in the transverse direction. The three slip ratios, 2°, 4°, and 6° were referred to as FR2, FR4, and FR6, respectively, in the figures below. Figure 4-5 illustrates the typical variations of the contact stresses in the three orthogonal directions along the second meridian of Rib 3 considering $V = 8 \text{ km/h}$, $P = 44.4 \text{ kN}$, and $\sigma_0 = 690 \text{ kPa}$. This location was selected as the representative meridian as high stress concentrations was anticipated at the inner part of the tire relative to the cornering condition.





(c)

Figure 4-5. Typical contact stress variation of a cornering tire with $V = 8 \text{ km/h}$, $P = 44.4 \text{ kN}$, and $\sigma_0 = 690 \text{ kPa}$ in the (a) vertical, (b) longitudinal, and (c) transverse directions.

For the vertical contact stresses, their corresponding magnitudes along the contact length increased as the slip angle increased from 2° to 6° , although the difference between 4° and 6° seemed to be minimal. The resulting longitudinal contact stresses indicated some slight variations from the free-rolling condition, but the values were arguably small – wherein the scale of the stress values was lower by one magnitude. This indicated that the impact of longitudinal contact stresses on pavement responses was significantly lower than the stresses in the other two orthogonal directions.

In addition, one could observe the manifestation of the concentration at the inner part of the tire based on Figure 4-6. At $P = 26.7 \text{ kN}$, there was a slight increase on the cumulative vertical forces per meridian along the rib width, predominantly at Rib 1 (inner rib). This behavior was exacerbated as the applied load was further increased to 44.4 kN , as there was a steep increase closer to the inner tire edge.

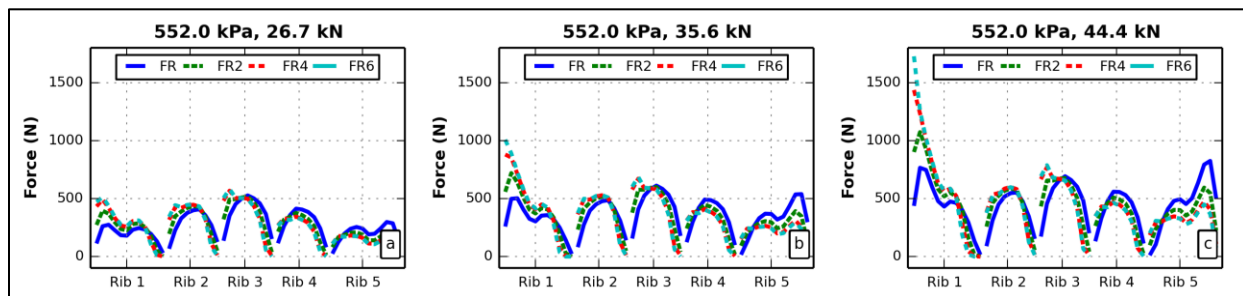


Figure 4-6. Vertical force distribution carried by each meridian for a cornering tire with $\sigma_0 = 552 \text{ kPa}$ and $V = 8 \text{ km/h}$ with varying applied loads.

As anticipated, the transverse contact stresses were greatly impacted by the cornering condition. The negative peak at the rear end of the tire quickly switched sign to positive when the slip angle was changed from the zero slip angle condition to 2° , Figure 4-5(c). In addition, closer to the trailing end, this part of the contact patch reached the limit imposed by the friction coefficient as the points of the curves were coincidental on this region. An increment increase of 2° further

pushed the transverse contact stress distribution to reach the interfacial friction limit. It can be observed that more points from the cases considering 4° and 6° are on the exact trajectory.

In reference to Appendix D, as the linear speed was increased, the transverse contact stress distribution was decreased and the relative difference between the cases with 4° and 6° was further minimized. A relatively smaller reduction in the peaks of the longitudinal contact stresses was also observed with increasing translational velocity, while the vertical stress distributions remained unaffected.

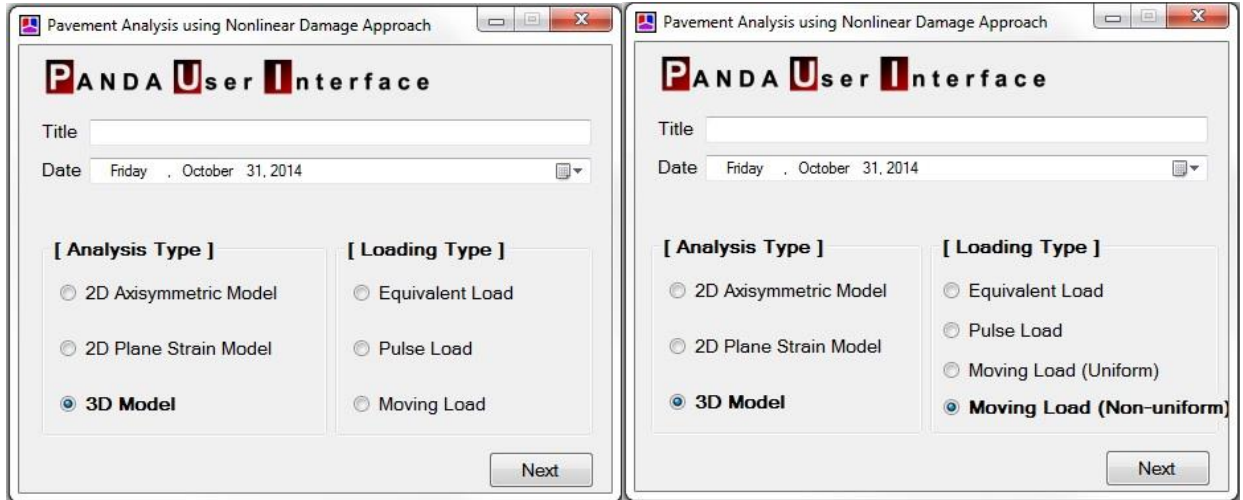
5 IMPLEMENTATION OF CONTACT STRESSES INTO PANDA

PUI is an interface generating the FE input file of pavements for PANDA based on the user's input information. PUI receives input data such as analysis type, loading type, depth of layers, material properties of each layer, loading magnitude and conditions from an engineer and generates the pavement FE input file. Previous version of PUI generates a pavement FE model, which applies the vertical pressure uniformly on the pavement. In this work PUI is revised to receive the information of applied load, tire inflation pressure, vehicle speed, rolling condition, and slip ratio/angle from the user and apply the corresponding 3-D non-uniform contact stresses obtained from simulations in the previous sections on the pavement model.

5.1 REVISED FEATURES

Tire contact stresses induced by the tire on pavement depend on many factors. Tire inflation pressure, vehicle speed, vehicle rolling condition, and slip ratios change the tire contact stresses for a constant applied load. The produced database in the previous sections was incorporated into the PUI, Figure 1-2. Therefore, a user can choose a realistic scenario of tire and driving conditions. PUI automatically applies the corresponding tire contact stresses obtained from numerical simulations on pavements.

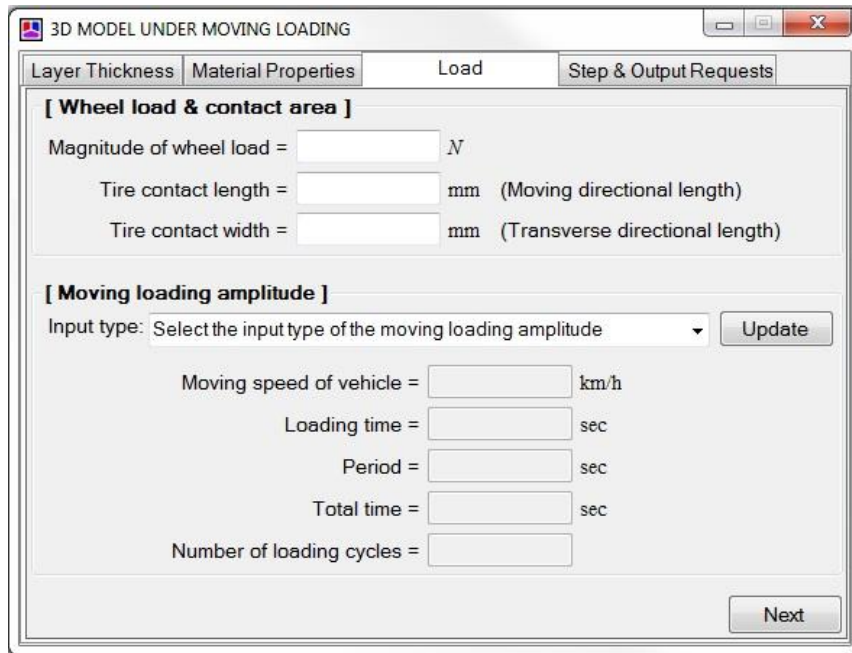
Figure 5-1 (a) and (b) demonstrate the main window of PUI in the previous and new versions. This window provides user options on the analysis and loading types. In the previous version of PUI, the user could choose between three different loading types: equivalent, pulse, and moving load, as shown in Figure 5-1(a). In the main window of the new version of PUI, the user is provided with an additional option, which is a non-uniform moving load, as shown in Figure 5-1(b). Figure 5-2(a) and (b) illustrate the load tab of PUI in the previous and new versions. The load tab in the new version of PUI changes according to the user's choice in the main window. If a user chooses the uniform moving load in the main window, the load tab of the previous version of PUI pops up, as shown in Figure 5-2(a); if a user chooses the non-uniform moving load, the load tab of the new version appears, as shown in Figure 5-2(b). The load tab in the new version provides user with options of tire and vehicle conditions. Figure 5-3(a)-(e) demonstrate the available options for a user to choose the applied load, tire pressure, vehicle speed, rolling condition, and slip ratio based on available data in the produced database. Then, PUI automatically applies the corresponding non-uniform 3-D contact stresses on the generated FE representation of the pavement.



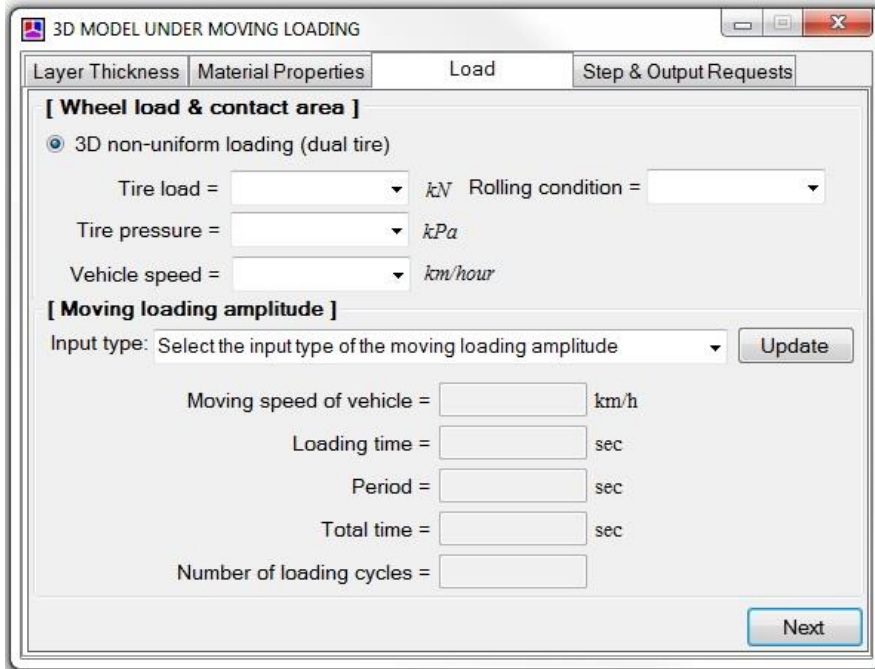
(a)

(b)

Figure 5-1. The main window of PUI in the (a) previous version and (b) new version to select analysis and loading types.

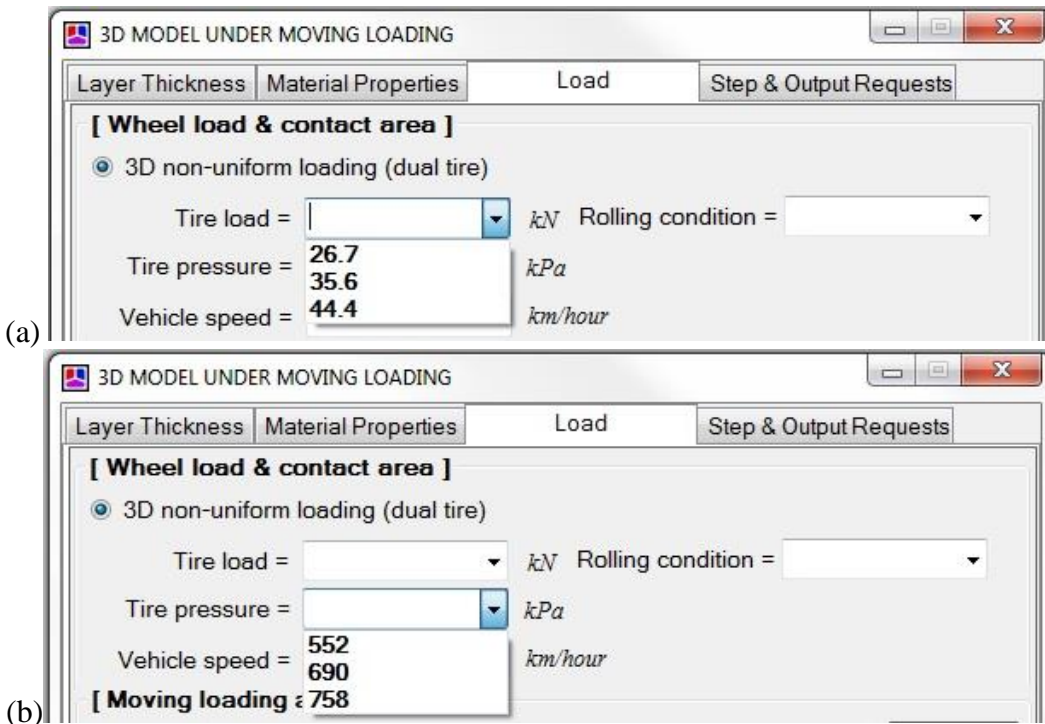


(a)



(b)

Figure 5-2. The load tab of PUI in the (a) previous version and (b) new version to select load and contact area.



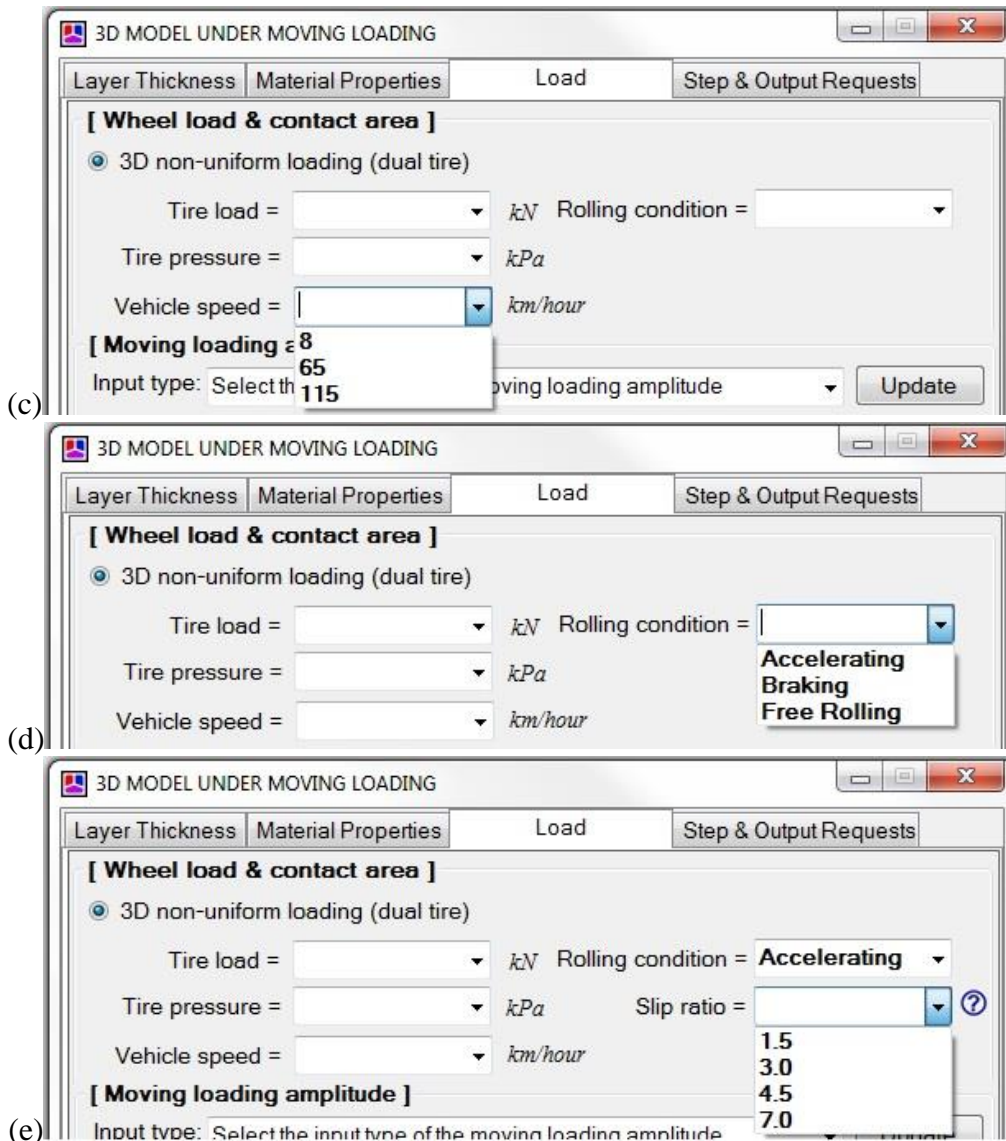


Figure 5-3. Available options of PUI to choose (a) tire load, (b) tire pressure, (c) vehicle speed, (d) rolling conditions, and (e) slip ratio.

5.2 ALGORITHM AND APPROACH

The previous version of PUI applies uniform loading on pavement. The uniform vertical pressure is moving along the wheel path of the pavement FE model by half-length overlapping of the tire contact length. Figure 5-4 demonstrates the longitudinal dimensions of the pavement FE model. The effective longitudinal contact length is denoted by X . The wheel moving distance is considered to be $7X$. Then, the length of the FE model is $9X$, including $1X$ of redundant FE model at each side. Consequently, the total longitudinal length of the model including infinite boundaries at both ends becomes $16X$. Figure 5-5(a) demonstrates a sample of the generated FE input file by PUI for uniform moving load. Figure 5-5(b) and (c) illustrate the uniform mesh and uniform vertical pressure on the surface of the pavement FE model. It can be seen that the area of elements are the same on the surface of pavements. The default number of elements in the moving direction for

load to be applied on it is 8 elements. The length of the elements changes according to the user input for the tire contact length. The number of elements in the transverse direction under the tire contact stresses changes according to the tire contact width from 1 to 13 elements. Because the half-length overlapping of the discretized moving wheel load is used in PUI, 13 rectangular sets are defined and the load is applied on these sets, as shown in Figure 5-5(d).

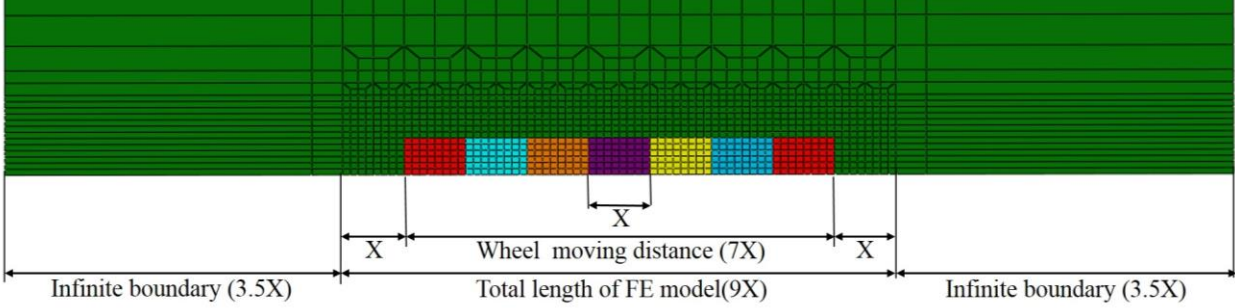
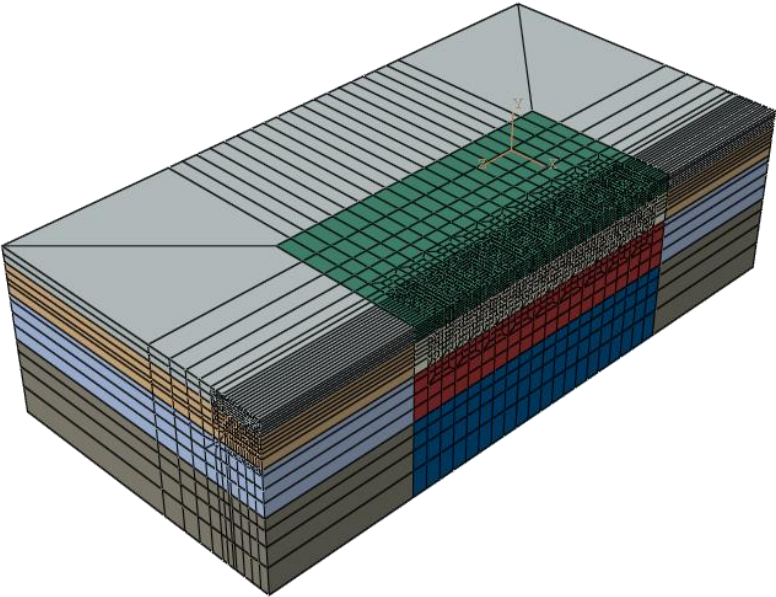
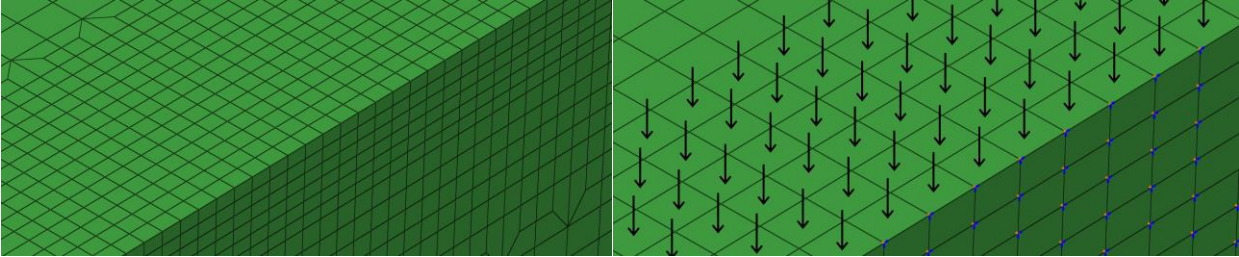


Figure 5-4. Longitudinal dimensions of the finite element model.

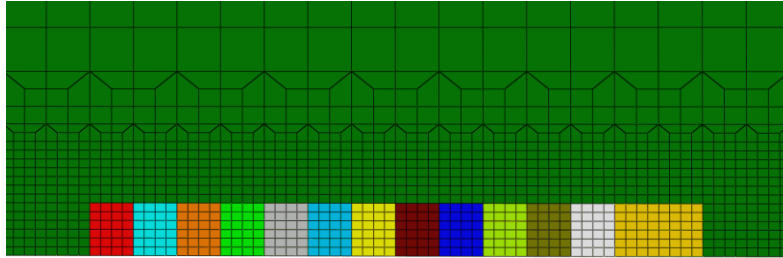


(a)



(b)

(c)



(d)

Figure 5-5. Characteristics of FE model for uniform moving load, (a) four-layer pavement FE model, (b) uniform meshing under the wheel path, (c) uniform vertical pressure on the surface, and (d) 13 different defined sets for applied load.

In order to incorporate the 3-D non-uniform tire contact stresses and produce the corresponding FE input file, PUI was revised in different aspects.

First, the widths and lengths of the elements in the pavement FE model were revised according to the contact area obtained from numerical results of tire simulations. A total of 16 elements were considered in the transverse direction to accommodate the number of ribs and grooves of a dual tire. The widths of these elements were revised to be defined according to the ribs and grooves sizes of each tire condition and configuration obtained from numerical results. In the moving direction eight elements, similar to the uniform loading case, were considered for tire contact length and their length changes according to the tire contact length obtained from tire simulations. Figure 5-6(b) demonstrates a sample of generated mesh on the surface of the pavement FE model.

Second, the 3-D contact stresses obtained from numerical results were applied on the pavement. For this purpose, in addition to vertical pressure, surface traction boundary conditions were defined and applied on the pavements surface. The traction types of loadings, transverse and longitudinal contact stresses, and their directions were defined to be applied on the pavement. Figure 5-6(c) illustrates a sample of the 3-D non-uniform loading applied on the pavement's model.

Third, the defined sets on the surface of the pavement FE model were revised to accommodate non-uniform loadings. The 13 sets on the surface were not enough to apply the non-uniform contact stresses obtained from tire simulations on the pavement. Therefore, as many sets as the number of elements on the wheel path, $8 \times 12 \times 13$ sets, were defined. Figure 5-6(d) demonstrates the defined sets in the new pavement FE model.

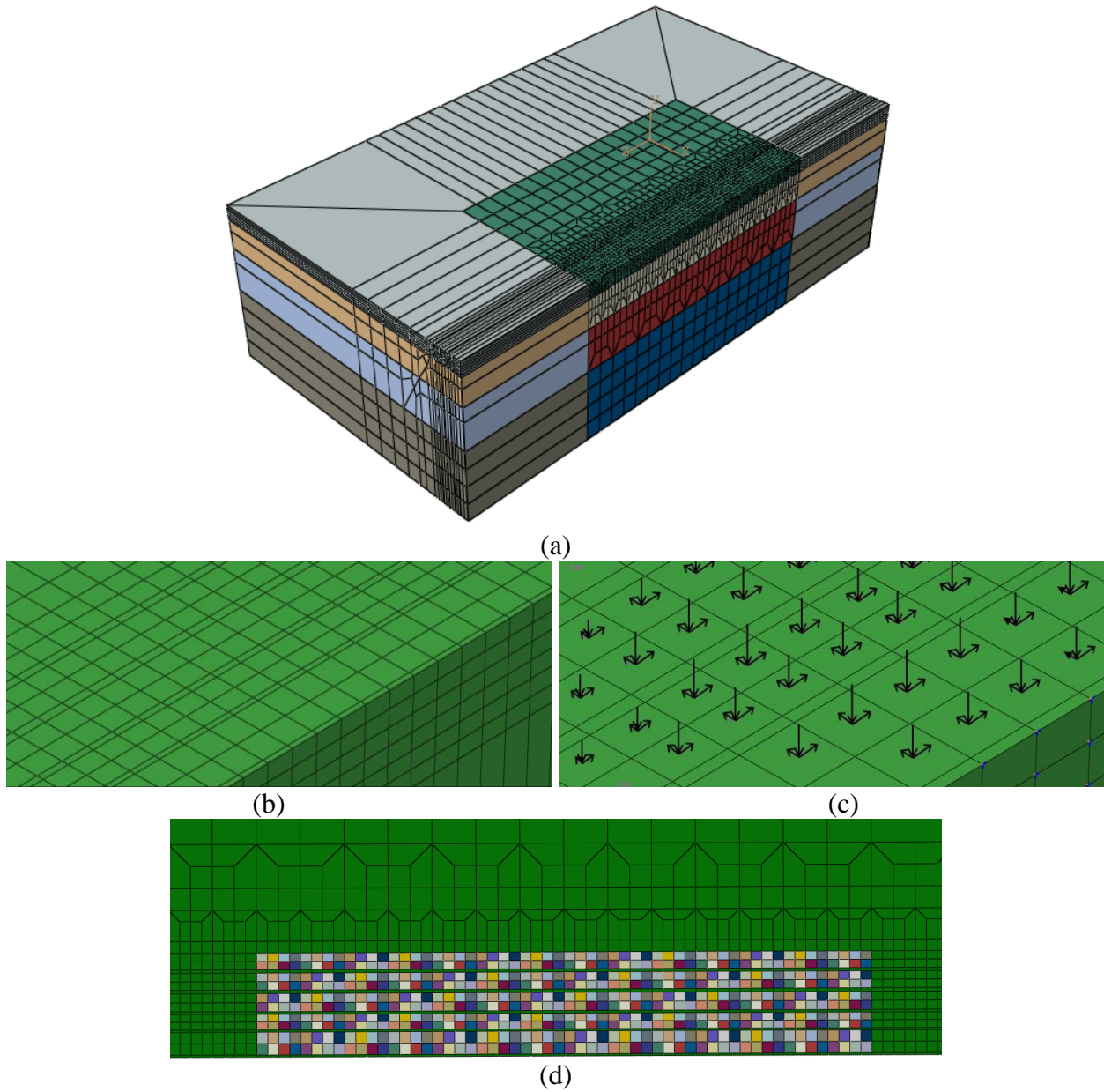
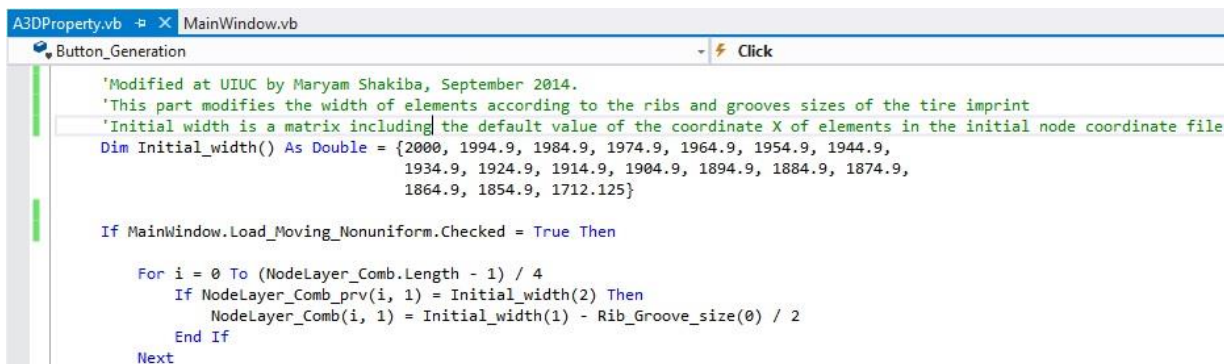


Figure 5-6. Characteristics of the FE model for 3-D non-uniform moving load, (a) four-layer pavement FE model, (b) non-uniform meshing under the wheel path, (c) 3-D non-uniform contact stresses on the surface, and (d) +1000 defined sets for non-uniform contact stresses to be applied on.

More than 300 text files, including the contact area and 3-D non-uniform contact stresses obtained from tire simulations, were added to the PUI resource files. The contact area consists of information on the rib and groove sizes in addition to the tire contact length. According to the user-selected cases, PUI automatically uses the corresponding file and inserts contact stresses and revises element sizes. It should be mentioned that half of the dual tire (i.e., one tire) was incorporated in these FE input file generations to maintain consistency with the available PUI structure.

5.3 IMPLEMENTATION

PUI was written using Visual Studio code (2012). This code was modified in this work to consider the explained revisions. Comments were written in the code indicating the date of modification and a brief description of the modifications that has been implemented, as shown in Figure 5-7. To revise the width of the element, if-clauses were added to the code to modify the default value of nodes' coordinates according to the rib and groove sizes, as shown in Figure 5-7. The default value of the x coordinate of nodes, coordinate in the transverse direction, were saved in a matrix, Initial_width, obtained from resource files in PUI and then revised accordingly. Sets were defined based on the label of element on the surface of pavements and a sample of lines defining one set is demonstrated in Figure 5-8. The contact stresses were called from the load matrix and applied on the defined sets, as shown in Figure 5-9.

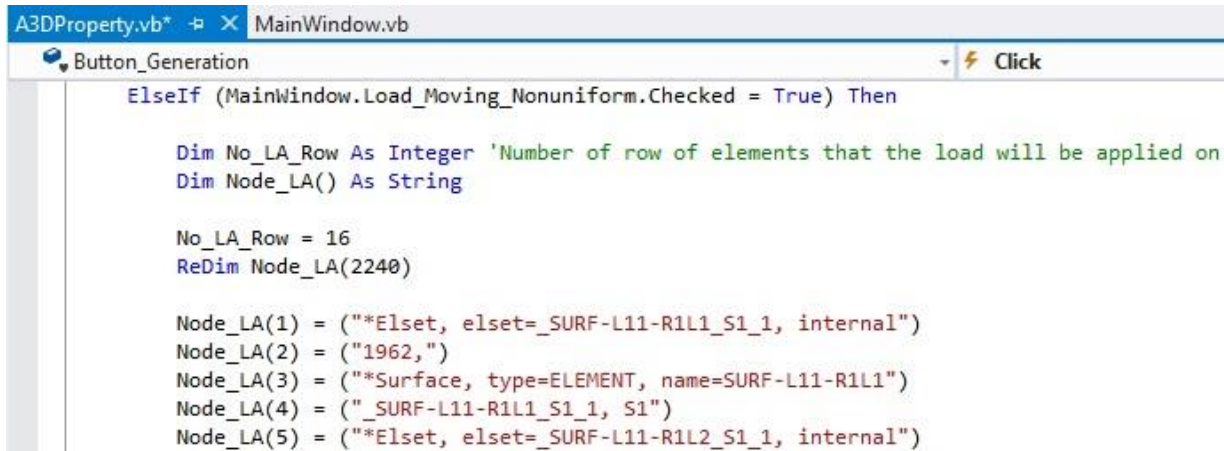


```
A3DProperty.vb * X MainWindow.vb
Button_Generation Click
'Modified at UIUC by Maryam Shakiba, September 2014.
'This part modifies the width of elements according to the ribs and grooves sizes of the tire imprint
'Initial width is a matrix including the default value of the coordinate X of elements in the initial node coordinate file
Dim Initial_width() As Double = {2000, 1994.9, 1984.9, 1974.9, 1964.9, 1954.9, 1944.9,
                                1934.9, 1924.9, 1914.9, 1904.9, 1894.9, 1884.9, 1874.9,
                                1864.9, 1854.9, 1712.125}

If MainWindow.Load_Moving_Nonuniform.Checked = True Then

    For i = 0 To (NodeLayer_Comb.Length - 1) / 4
        If NodeLayer_Comb_prv(i, 1) = Initial_width(2) Then
            NodeLayer_Comb(i, 1) = Initial_width(1) - Rib_Groove_size(0) / 2
        End If
    Next
```

Figure 5-7. Part of the modified visual studio code demonstrating an explanation comment and an if-clause modifying elements width value.



```
A3DProperty.vb * X MainWindow.vb
Button_Generation Click

ElseIf (MainWindow.Load_Moving_Nonuniform.Checked = True) Then

    Dim No_LA_Row As Integer 'Number of row of elements that the load will be applied on
    Dim Node_LA() As String

    No_LA_Row = 16
    ReDim Node_LA(2240)

    Node_LA(1) = ("*Elset, elset=_SURF-L11-R1L1_S1_1, internal")
    Node_LA(2) = ("1962,")
    Node_LA(3) = ("*Surface, type=ELEMENT, name=SURF-L11-R1L1")
    Node_LA(4) = ("_SURF-L11-R1L1_S1_1, S1")
    Node_LA(5) = ("*Elset, elset=_SURF-L11-R1L2_S1_1, internal")
```

Figure 5-8. A Visual Studio code defining new sets to applied non-uniform load.

```

A3DProperty.vb  MainWindow.vb
Button_Generation  Click

'Modified at UIUC by Maryam Shakiba, August 2014.
'This part Produces the loading lines of input file for non-uniform load applied on the surface
'Load_Line_3D is a matrix including the 3D non-uniform contact stresses
Dim Load_name_P1() As String = {"** Name: Load-1-P  Type: Pressure"}
Dim DsLoad_P1() As String = {"**Dsload, amplitude=Amp-1"}
Dim Load_P1_Temp_L11_P11() As String = {"A3DM.Surf-L11-R1L1,P", Load_Line_3D(0, 0)}
Dim Load_P1_Temp_L11_P12() As String = {"A3DM.Surf-L11-R1L2,P", Load_Line_3D(0, 1)}
Dim Load_P1_Temp_L11_P13() As String = {"A3DM.Surf-L11-R1L3,P", Load_Line_3D(0, 2)}
Dim Load_P1_Temp_L11_P14() As String = {"A3DM.Surf-L11-R1L4,P", Load_Line_3D(0, 3)}

A3DProperty.vb  MainWindow.vb
Button_Generation  Click

Dim Load_name_TL1() As String = {"** Name: Load-1-TL  Type: Surface traction"}
Dim DsLoad_TL1() As String = {"**Dsload, amplitude=Amp-1"}
Dim Load_TL1_Temp_L11_TL11() As String = {"A3DM.Surf-L11-R1L1,TRSHR", Load_Line_3D(10, 0), "0,0,-1"}
Dim Load_TL1_Temp_L11_TL12() As String = {"A3DM.Surf-L11-R1L2,TRSHR", Load_Line_3D(10, 1), "0,0,-1"}
Dim Load_TL1_Temp_L11_TL13() As String = {"A3DM.Surf-L11-R1L3,TRSHR", Load_Line_3D(10, 2), "0,0,-1"}
Dim Load_TL1_Temp_L11_TL14() As String = {"A3DM.Surf-L11-R1L4,TRSHR", Load_Line_3D(10, 3), "0,0,-1"}
Dim Load_TL1_Temp_L11_TL21() As String = {"A3DM.Surf-L11-R2L1,TRSHR", Load_Line_3D(11, 0), "0,0,-1"}
Dim Load_TL1_Temp_L11_TL22() As String = {"A3DM.Surf-L11-R2L2,TRSHR", Load_Line_3D(11, 1), "0,0,-1"}

A3DProperty.vb  MainWindow.vb
Button_Generation

Dim Load_Applied() As String
ReDim Load_Applied(3198)

Load_Applied(1) = ("** Name: Load-1-P  Type: Pressure")
Load_Applied(2) = ("**Dsload, amplitude=Amp-1")
Load_Applied(3) = Join(Load_P1_Temp_L11_P11, ",")
Load_Applied(4) = Join(Load_P1_Temp_L11_P12, ",")
Load_Applied(5) = Join(Load_P1_Temp_L11_P13, ",")
Load_Applied(6) = Join(Load_P1_Temp_L11_P14, ",")
Load_Applied(7) = Join(Load_P1_Temp_L11_P21, ",")

```

Figure 5-9. A Visual Studio code defining (a) vertical non-uniform pressure on defined sets, (b) non-uniform longitudinal traction on defined sets, and (c) concatenating the produced lines in (a) and (b) to be written in FE input file.

It should be mentioned that more changes were made inside the Visual Studio PUI code to accommodate all revisions. For example, modifications were made in the main window's code to produce the new non-uniform loading option and to automatically change the load tab. Other changes were made to modify the accurate flow of the code according to new choices provided to the user. These changes were explained in the comments inside the Visual Studio code to clarify all revisions.

6 FINDINGS AND CONCLUSIONS

The culmination of a validated finite element model of a truck tire provides an avenue to appropriately predict numerical contact stresses. Some important contributions of the research study is the combination of a detailed geometry, and laboratory-produced material properties for varying tire components of a dual-tire assembly. For instance, rubber was characterized as hyperelastic to account for its inherent large deformation behavior, and steel was considered to be elastic. A robust mesh sensitivity analysis also generated a suitable basis for validating and calibrating the tire model under steady-state conditions. Various checks, including deflection, contact area, and resultant force, also ensured that the model is numerically sound.

In addition, the analysis matrix included a broad range of applied loads, tire inflation pressures, linear speeds, and rolling conditions to account for realistic truck loading scenarios. Some key findings of the numerical contact stress analysis include the following:

- Velocity change does not impact contact stress variation in the three orthogonal directions for a free-rolling tire.
- For a constant applied load, with varying inflation pressure, the model is able to capture an increase of the maximum vertical contact stress. In addition, with a constant tire inflation pressure, increase in applied load does not affect the maximum vertical contact stress, instead the contact length is increased.
- For a free-rolling scenario, the increase in contact length led to the increase of the longitudinal stress peaks, as with the given condition, a greater leverage is provided for relative tread deformation.
- Both the accelerating and braking scenarios did not impact the vertical contact stresses significantly, although a slight shift away from the center is observed. For both rolling conditions, with increasing slip ratios, the trailing part of the tire reaches the interfacial friction limit faster than the remainder of the contact patch. Lastly, the range of values for the transverse contact stresses are significantly less than that of the vertical and longitudinal directions – which indicates that at the chosen “representative” meridian, the influence of transverse stresses is less than the stresses in the other two orthogonal directions.
- Longitudinal contact stresses indicated a slightly higher affinity to be influenced by the change in linear speed more so than the transverse values.
- The high lateral force generated during a cornering maneuver creates a concentration in the inner vicinity of the tire – leading to asymmetric contact stresses, more predominantly for the vertical and transverse directions. This was observed with the numerical simulations and in contrast to the accelerating and braking conditions, the longitudinal stresses values were lower by a magnitude than the stresses in other directions.
- Further increase of the slip angle past 4° indicates a slower rate of contact stress distribution increase, as most of the points generated with this slip angle are coincidental with ones with 6° . This can indicate that for the cornering condition, slip angles greater than 4° will have the tendency to reach the frictional limit between the tire and pavement surface.
- Similar to the accelerating and braking scenarios, the vertical stress distribution remain marginally affected by the change in translational speed.

With the validated tire model, a robust generation of representative numerical tire-pavement contact stresses becomes possible. Anticipated influences by main factors considered in the

analysis matrix were also observed – further strengthening the capability of the model to provide sufficient loading inputs for the PANDA simulations.

7 REFERENCES

- Al-Qadi, I.L., Yoo, P.J., 2007. Effect of Surface Tangential Contact Stresses on Flexible Pavement Response. *Journal of the Association of Asphalt Paving Technologists* 76, 663–692.
- Anghelache, G., Moisescu, R., Sorohan, Ş., Buretea, D., 2011. Measuring System for Investigation of Tri-axial Stress Distribution across the Tyre–Road Contact Patch. *Measurement* 44, 559-568.
- Anghelache, G., Negrus, E.M., Ciubotaru, O., 2003. Investigation of Shear Stresses in the Tire-Road Contact Patch. SAE Technical Paper.
- Bonse, R., Kuhn, S., 1959. Dynamic Forces Exerted by Moving Vehicles on a Road Surface. *Highway Research Board Bulletin*.
- Darabi, M.K., Abu Al-Rub, R.K., Masad, E.A., Huang, C.-W., Little, D.N., 2011. A thermo-viscoelastic–viscoplastic–viscodamage Constitutive Model for Asphaltic Materials. *International Journal of Solids and Structures* 48, 191-207.
- De Beer, M., Fisher, C., Jooste, F., 2002. Evaluation of Non-uniform Tyre Contact Stresses on Thin Asphalt Pavements, Ninth international conference on asphalt pavements (ICAP 2002), Copenhagen, Denmark, pp. 19-22.
- Drakos, C.A., Roque, R., Birgisson, B., 2001. Effects of Measured Tire Contact Stresses on Near-Surface Rutting. *Transportation Research Record: Journal of the Transportation Research Board* 1764, 59-69.
- Ghoreishy, M.H.R., Malekzadeh, M., Rahimi, H., 2007. A Parametric Study on the Steady State Rolling Behaviour of a Steel-Belted Radial Tyre. *Iranian Polymer Journal* 16, 539-548.
- Gruber, P., Sharp, R.S., 2012. Shear Forces in the Contact Patch of a Braked-Racing Tyre. *Vehicle System Dynamics* 50, 1761-1778.
- Gruber, P., Sharp, R.S., Crocombe, A.D., 2011a. Normal and Shear Forces in the Contact Patch of a Braked Racing Tyre. Part 1: Results from a Finite-Element Model. *Vehicle System Dynamics* 50, 323-337.
- Gruber, P., Sharp, R.S., Crocombe, A.D., 2011b. Normal and Shear Forces in the Contact Patch of a Braked Racing Tyre. Part 2: Development of a Physical Tyre Model. *Vehicle System Dynamics* 50, 339-356.
- Himeno, K., Kamijima, T., Ikeda, T., Abe, T., 1997. Distribution of Tire Contact Pressure of Vehicles and Its Influence on Pavement Distress, Eighth International Conference on Asphalt Pavements.
- Howell, W.E., Perez, S.E., Vogler, W.A., 1986. Aircraft Tire Footprint Forces. The tire Pavement Interface, ASTM STP 929, 110-124.
- Lippmann, S., Oblizajek, K., 1974. The Distributions of Stress between the Tread and the Road for Freely Rolling Tires. SAE Technical Paper.
- Masad, E., Rashid Abu Al-Rub, Little., D.N., 2012. Recent Developments and Applications of Pavement Analysis Using Nonlinear Damage (PANDA) Model., 7th RILEM International Conference on Cracking in Pavements, Springer Netherlands, pp. 399-408.
- Meng, L., 2002. Truck Tire/Pavement Interaction Analysis by the Finite Element Method. Michigan State University. Department of Materials Science and Mechanics.
- Pauwelussen, J., 2015. *Essentials of Vehicle Dynamics*. Elsevier.
- Romanoschi, S.A., Metcalf, J.B., 2001. Characterization of Asphalt Concrete Layer Interfaces. *Transportation Research Record: Journal of the Transportation Research Board* 1778, 132-139.

- Roque, R., Myers, L., Birgisson, B., 2000. Evaluating Measured Tire Contact Stresses to Predict Pavement Response and Performance. *Transportation Research Record: Journal of the Transportation Research Board* 1716, 73-81.
- Seitz, N., Hussmann, A., 1971. Forces and Displacement in Contact Area of Free Rolling Tires. SAE Technical Paper 710626.
- Shoop, S.A., 2001. Finite Element Modeling of Tire-Terrain Interaction. DTIC Document.
- Siddharthan, R., Krishnamenon, N., El-Mously, M., Sebaaly, P., 2002. Investigation of Tire Contact Stress Distributions on Pavement Response. *Journal of Transportation Engineering* 128, 136-144.
- Tielking, J., Roberts, F., 1987. Tire Contact Pressure and Its Effect on Pavement Strain. *Journal of Transportation Engineering* 113, 56-71.
- Tielking, J.T., Abraham, M.A., 1994. Measurement of Truck Tire Footprint Pressures. *Transportation research record*.
- Wang, G., Roque, R., 2010. Three-Dimensional Finite Element Modeling of Static Tire-Pavement Interaction. *Transportation Research Record: Journal of the Transportation Research Board* 2155, 158-169.
- Wang, H., Al-Qadi, I., Stanciulescu, I., 2014. Effect of Surface Friction on Tire–Pavement Contact Stresses during Vehicle Maneuvering. *Journal of Engineering Mechanics* 140, 04014001.
- Wang, H., Al-Qadi, I.L., 2009. Combined Effect of Moving Wheel Loading and Three-Dimensional Contact Stresses on Perpetual Pavement Responses. *Transportation Research Record: Journal of the Transportation Research Board* 2095, 53-61.
- Wang, H., Al-Qadi, I.L., 2010. Evaluation of Surface-Related Pavement Damage due to Tire Braking. *Road Materials and Pavement Design* 11, 101-121.
- Wang, H., Al-Qadi, I.L., Stanciulescu, I., 2011. Simulation of Tyre–Pavement Interaction for Predicting Contact Stresses at Static and Various Rolling Conditions. *International Journal of Pavement Engineering* 13, 310-321.
- Wong, J.Y., 2008. *Theory of Ground Vehicles*. 4th Edition, John Wiley, New York.
- Yap, P., 1988. A Comparative Study of the Effect of Truck Tire Types on Road Contact Pressures. SAE Technical Paper.
- Zhang, X., Rakheja, S., Ganesan, R., 2001. Estimation of Tyre-Road Contact Pressure Distribution Based on Nonlinear Finite Element Analysis. *International Journal of Heavy Vehicle Systems* 8, 197-217.

